

INTERMODULATION DISTORTIONS FROM A CHAIN OF COUPLED NONLINEAR
OSCILLATORS NEAR A HOPF BIFURCATION



A Thesis Submitted in Partial Fulfillment of the Requirements
for the Degree of Master of Science in Physics
Department of Physics
FACULTY OF SCIENCE
Chulalongkorn University
Academic Year 2020
Copyright of Chulalongkorn University



จุฬาลงกรณ์มหาวิทยาลัย
CHULALONGKORN UNIVERSITY

สัญญาฉบับนี้เป็นแบบอินเตอร์มอดูเลชั่นจากระบบของตัวสันแบบไม่เชิงเส้นที่แสดงการแยกแบบ
ฮอปฟ์



วิทยานิพนธ์นี้เป็นส่วนหนึ่งของการศึกษาตามหลักสูตรปริญญาวิทยาศาสตรมหาบัณฑิต
สาขาวิชาฟิสิกส์ ภาควิชาฟิสิกส์
คณะวิทยาศาสตร์ จุฬาลงกรณ์มหาวิทยาลัย
ปีการศึกษา 2563
ลิขสิทธิ์ของจุฬาลงกรณ์มหาวิทยาลัย

Thesis Title INTERMODULATION DISTORTIONS FROM A CHAIN OF
COUPLED NONLINEAR OSCILLATORS NEAR A HOPF
BIFURCATION

By Mr. Yanathip Thipmaungprom

Field of Study Physics

Thesis Advisor Yuttana Roongthumskul

Accepted by the FACULTY OF SCIENCE, Chulalongkorn University in Partial
Fulfillment of the Requirement for the Master of Science

..... Dean of the FACULTY OF SCIENCE
(Professor POLKIT SANGVANICH)

THESIS COMMITTEE

..... Chairman
(Associate Professor NAKORN PHAISANGITTISAKUL)

..... Thesis Advisor
(Yuttana Roongthumskul)

..... Examiner
(Assistant Professor Varagorn Hengpunya)

..... External Examiner
(Assistant Professor Sujint Suwanna)

ญานาธิป ทิพย์เมืองพรหม : สัญญาณบิตเป็นแบบอินเทอร์มอดูเลชันจากระบบของตัวสั่นแบบไม่เชิงเส้นที่แสดงการแยกแบบฮอปฟ์. (INTERMODULATION DISTORTIONS FROM A CHAIN OF COUPLED NONLINEAR OSCILLATORS NEAR A HOPF BIFURCATION) อ.ที่ปรึกษาหลัก : อ. ดร.ยุทธนา รุ่งธรรมสกุล

หูชั้นในสามารถสร้างเสียงสะท้อนที่มีความถี่สอดคล้องกับผลรวมเชิงเส้นของความถี่ของเสียงกระตุ้น f_1 และ f_2 ได้ โดยเสียงสะท้อนนี้เรียกว่าเสียงสะท้อนจากหูชั้นในแบบดีพีโอเออี (Distortion Product Otoacoustic Emissions, DPOAEs) ซึ่งสามารถตรวจวัดได้โดยการใช้ไมโครโฟนสอดเข้าไปในรูหู ในมนุษย์นั้นระดับความเข้มของเสียงดีพีโอเออีที่ความถี่ $2f_1-f_2$ มีการเปลี่ยนแปลงขึ้นอยู่กับความถี่ของเสียงกระตุ้นและสามารถแสดงลักษณะแบบกึ่งคาบ (quasi-periodic) ที่เรียกว่าโครงสร้างละเอียดของเสียงสะท้อนจากหูชั้นในแบบดีพีโอเออี (DPOAE fine structure) ได้ ปรากฏการณ์ดังกล่าวเป็นที่ยอมรับโดยทั่วไปว่าเกิดจากผลของการแทรกสอดกันของสัญญาณเสียงดีพีโอเออีสองสัญญาณที่มาจากกลุ่มของเซลล์ขนที่มีค่าความถี่จำเพาะสอดคล้องกับความถี่ของเสียงกระตุ้นและความถี่ของสัญญาณบิตเป็น อย่างไรก็ตามจากผลการศึกษาที่ผ่านมา พบว่าระดับโครงสร้างละเอียดนี้สามารถพบได้ในกบนาซึ่งมีโครงสร้างของหูชั้นในที่ไม่รองรับสมมติฐานการเกิดการแทรกสอดระหว่างสัญญาณเสียงดีพีโอเออีสองสัญญาณ เนื่องจากเซลล์ขนที่อยู่ภายในร่างกายของสัตว์สะเทินน้ำสะเทินบกมีการเชื่อมต่อกันอย่างแน่นหนา ในการศึกษาวิจัยครั้งนี้ ผู้จัดทำได้ใช้ระบบของตัวสั่นแบบไม่เชิงเส้นในหนึ่งมิติที่มีการเชื่อมต่อกันอย่างแน่นหนาซึ่งเป็นโครงสร้างที่แสดงถึงเซลล์ขนภายในหูชั้นในอย่างง่ายเพื่อจำลองการเกิดสัญญาณบิตเป็นแบบอินเทอร์มอดูเลชัน ผลการจำลองพบว่าแอมพลิจูดของเสียงดีพีโอเออีที่สร้างจากระบบของตัวสั่นที่ตัวสั่นมีการเรียงตัวตามลำดับของค่าความถี่จำเพาะของแต่ละตัวสั่นแบบเชิงเส้นสามารถแสดงลักษณะแบบกึ่งคาบได้เมื่อระดับของแรงกระตุ้นมีค่าเหมาะสม ผลการวิเคราะห์การตอบสนองของตัวสั่นแต่ละตัวในระบบแสดงให้เห็นว่าการตอบสนองจากตัวสั่นที่มีค่าความถี่จำเพาะต่ำได้รับผลจากคลื่นนิ่งซึ่งเป็นส่วนสำคัญต่อการเกิดลักษณะแบบกึ่งคาบ ในทางกลับกันระบบของตัวสั่นที่มีการเรียงตัวตามลำดับของค่าความถี่จำเพาะของแต่ละตัวสั่นแบบสุ่มแสดงการตอบสนองที่คล้ายคลึงกับตัวสั่นแบบไม่เชิงเส้นหนึ่งตัว โดยผลจากแบบจำลองที่ได้มีความสอดคล้องเชิงคุณภาพกับผลที่พบจากการทดลองที่ผ่านมา ผลการศึกษานี้ผู้จัดทำได้นำเสนอกลไกสำหรับอธิบายกระบวนการพื้นฐานของการเกิดเสียงสะท้อนจากหูชั้นในแบบดีพีโอเออีในกบนาซึ่งถูกควบคุมโดยรูปแบบการจัดเรียงตัวของเซลล์รับเสียง

CHULALONGKORN UNIVERSITY

สาขาวิชา ฟิสิกส์
ปีการศึกษา 2563

ลายมือชื่อนิสิต
ลายมือชื่อ อ.ที่ปรึกษาหลัก

6171939823 : MAJOR PHYSICS

KEYWORD: Hopf bifurcation, nonlinear oscillators, intermodulation distortions, auditory system, otoacoustic emissions

Yanathip Thipmaungprom : INTERMODULATION DISTORTIONS FROM A CHAIN OF COUPLED NONLINEAR OSCILLATORS NEAR A HOPF BIFURCATION. Advisor: Yuttana Roongthumskul

The inner ear can produce sounds whose frequencies correspond to linear combinations of the stimulus frequencies, f_1 and f_2 . These sounds, called Distortion Product Otoacoustic Emissions (DPOAEs), can be measured by inserting a microphone into the ear canal. In human, the intensity level of DPOAEs at frequency $2f_1 - f_2$ varies significantly with a stimulus frequency and can exhibit a quasi-periodic pattern, a feature termed a DPOAE fine structure. This distinctive characteristic has been generally accepted as a consequence of the interference between two DPOAE signals produced by two spatially separated groups of sensory hair cells, whose characteristic frequencies correspond to the stimulus frequencies, and the distortion frequency. However, a recent study revealed that a similar feature can be observed from Chinese edible frogs, whose inner ear structure does not support the two-signal interference hypothesis as *in vivo* amphibian hair cells are strongly coupled. In this work, we performed numerical simulations of nonlinear distortions produced by a chain of strongly coupled nonlinear oscillators, a structure that represents hair cells in a simple inner ear. Our results revealed that the amplitude of the total distortion from the oscillators, arranged in order of their characteristic frequencies, can display a quasiperiodic variation pattern under appropriate driving forces levels. Analyses of the motion of individual oscillators showed that those with low characteristic frequencies underwent a standing wave at the distortion frequency, a feature that was responsible for the quasiperiodic pattern. On the other hand, coupling between oscillators arranged in a random order of characteristic frequencies yielded a nonlinear response resembling that of a single oscillator. Results from the model agreed qualitatively with prior experimental observations. Our results thus suggest multiple mechanisms underlying DPOAEs produced by the frog's ear, governed by the arrangement of the sensory cells.

Field of Study: Physics

Student's Signature

Academic Year: 2020

Advisor's Signature

ACKNOWLEDGEMENTS

First and foremost, I would like to acknowledge my advisor Dr. Yuttana Roongthumskul for his valuable suggestions and comments on this project.

I would like to thank Assoc. Prof. Udomsilp Pinsook, Assoc. Prof. Thiti Bovornratanaraks, and Wisit Leelasiriwong for providing me the laboratory facility during this project.

I would like to thank Assoc. Prof. Nakorn Phaisangittisakul, Asst. Prof. Varagorn Hengpunya, and Asst. Prof. Sujin Suwanna for their contribution as chairman, examiner, and external examiner for my thesis defense with many invaluable suggestions and editing this work.

I would like to thank Department of Physics, Faculty of Science, Chulalongkorn University for providing me the facility during this project.

Last, but certainly not least, I would like to thank for the scholarship supported by Junior Science Talent Project (JSTP).

Yanathip Thipmaungprom

TABLE OF CONTENTS

	Page
.....	iii
ABSTRACT (THAI).....	iii
.....	iv
ABSTRACT (ENGLISH).....	iv
ACKNOWLEDGEMENTS.....	v
TABLE OF CONTENTS.....	vi
LIST OF FIGURES.....	ix
CHAPTER 1 INTRODUCTION.....	1
1.1 Motivation.....	1
1.2 Objectives.....	3
1.3 Scope of this research.....	4
1.4 Procedures.....	4
1.4.1 Literature review and define an objective of the study.....	4
1.4.2 Create a mathematical model to describe the generation of DPOAEs.....	4
1.4.3 Numerical simulations and analyses.....	4
1.4.4 Comparison of the simulation results with the experimental results, conclusion of the study, and writing the thesis.....	5
1.5 Expected outcome.....	5
1.6 Overview.....	5
CHAPTER 2 THEORETICAL BACKGROUND AND LITERATURE REVIEWS.....	6
2.1 The physiology of the vertebrate inner ear.....	6

2.2 Anatomy of the frog's inner ear.....	9
2.3 Otoacoustic emissions.....	10
2.4 Derivation of a nonlinear oscillator displaying a supercritical Hopf bifurcation	11
2.5 Verification of supercritical Hopf bifurcation	15
2.4 Mathematical model of the inner ear based on nonlinear oscillators.....	16
CHAPTER 3 METHODS	18
3.1 Derivation of a chain of coupled Hopf oscillators equation.....	18
3.2 A model of a chain of coupled nonlinear oscillators	19
3.3 Data analysis.....	20
3.4 Parameters selection.....	21
CHAPTER 4 RESULTS AND DISCUSSION	22
4.1 Response from a single Hopf oscillator.....	22
4.2 Determination of critical control parameter of a chain of coupled Hopf oscillators	24
4.3 The total IMDs from a chain of uncoupled Hopf oscillators	26
4.4 The total IMDs from a chain of coupled Hopf oscillators	30
4.4.1 Quasi-periodic amplitude variation pattern	30
4.4.2 Effects of the internal structure of the chain	36
4.4.2.1 Effect of coupling magnitude.....	36
4.4.2.2 Effect of oscillators number.....	38
4.4.2.3 Effect of oscillator's characteristic frequencies organization	39
4.5 Comparison with experimental measurements.....	41
4.6 Limitations of the model.....	42
CHAPTER 5 CONCLUSION	44

REFERENCES	47
APPENDIX A	51
APPENDIX B	55
VITA.....	57



LIST OF FIGURES

	Page
Figure 1.1 Sound pressure level spectrum recorded from mouse inner ear.....	1
Figure 1.2 Response amplitude of a single nonlinear oscillator.....	2
Figure 1.3 The amplitude of IMD recorded from a human subject.	3
Figure 2.1 The physiology of the vertebrate ear and inner ear.	6
Figure 2.2 Response of a hair bundle with and without a driving force.	8
Figure 2.3 Nonlinear properties of a hair bundle.....	9
Figure 2.4 Diagram of a supercritical Hopf bifurcation.....	16
Figure 4.1 Response amplitude and compressive nonlinearity from a single oscillator.	22
Figure 4.2 Effect of driving forces on a single oscillator.	23
Figure 4.3 Determination of critical control parameter.	25
Figure 4.4 Characteristic frequency of each oscillator.	26
Figure 4.5 Amplitude of the total IMD from a system of uncoupled oscillators.....	27
Figure 4.6 Oscillator's response from a system of uncoupled oscillators.	28
Figure 4.7 Polar plots of oscillator's response.	30
Figure 4.8 Amplitude of total IMDs from a system of coupled oscillators	31
Figure 4.9 Oscillator's response from a system of coupled oscillators.	32
Figure 4.10 The quasiperiodic variation in the IMD amplitude.	33
Figure 4.11 Oscillator's response from a different driving forces level.....	35
Figure 4.12 Effect of coupling magnitude to a system of coupled oscillators.	37
Figure 4.13 Effect of oscillators number to a system of coupled oscillators.	39

Figure 4.14 Effect of oscillator's characteristic frequencies organization. 40

Figure 4.15 Comparison between simulation and experimental results. 42



CHAPTER 1

INTRODUCTION

1.1 Motivation

Upon driven by two forces of different frequencies (denoted by f_1 and f_2), the displacement of a nonlinear oscillator can exhibit components at linear combinations of f_1 and f_2 . These signals, termed intermodulation distortions (IMDs), are general characteristics of nonlinear systems, and can be found typically in audio equipment such as amplifier or the recording system [1]. IMDs can be produced by the auditory system [2, 3]. The ear emits an outgoing acoustic wave at frequencies corresponding to the intermodulation distortions in response to sounds of two tones (Fig. 1.1). If the inner ear is assumed to be a time-invariant system, the intermodulation distortions should be accounted for by the nonlinearity of its internal process.

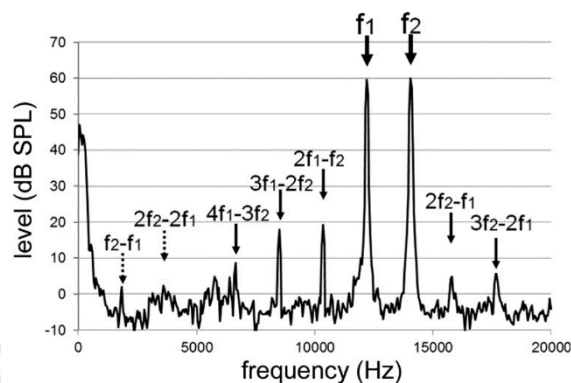


Figure 1.1 Sound pressure level spectrum recorded from mouse inner ear upon stimulated by 60-dB sounds at frequencies f_1 and f_2 . Intermodulation distortions can be observed at linear combinations of f_1 and f_2 [3].

Signal detection of the inner ear is performed by hair cells, the biological acoustic sensors of the auditory system. Several experimental studies have demonstrated that hair cells' vibrations evoked by an acoustic stimulus display strong nonlinearity. Upon driven by a sinusoidal force, the oscillation amplitude increases following a nonlinear function of the driving force magnitude ($A \sim F^{1/3}$). Hair cells also exhibit a frequency tuning behaviour whose quality factor decreases as the

driving force is elevated. The displacement of hair cell incorporates intermodulation distortions when driven by sinusoidal forces of multiple frequencies. Finally, under appropriate chemical environments, hair cells can spontaneously oscillate in the absence of an external force, a behaviour that parallels a limit-cycle oscillation displayed by a nonlinear oscillator poised near a bifurcation.

The amplitude of intermodulation distortions generated by a single nonlinear oscillator near a supercritical Hopf bifurcation driven by forces of two frequencies display a tuning characteristic. The peak amplitude is observed as the driving force frequencies approach the oscillator's characteristic frequency (Fig. 1.2) [4]. Similar behaviour was also found in the experimental results of a hair cell under an influence of two sinusoidal forces [5].

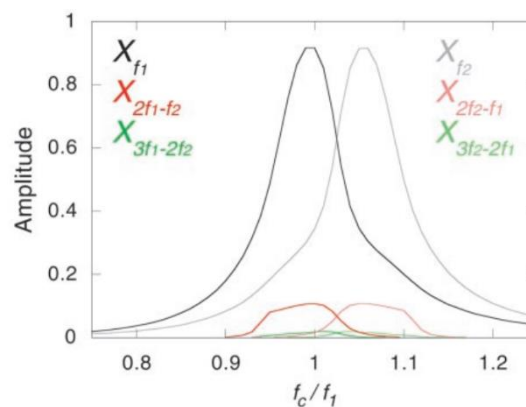


Figure 1.2 Response amplitude of a single nonlinear oscillator whose characteristic frequency is f_c to driving forces at frequencies f_1 and f_2 . The amplitude of IMDs at frequency $2f_1 - f_2$ (dark red line), $2f_2 - f_1$ (thin red line), $3f_1 - 2f_2$ (dark green line), and $3f_2 - 2f_1$ (thin green line) show a tuning behavior [4].

On the contrary, the sound pressure levels of intermodulation distortions from human subjects show quasi-periodic dependence on the stimulus frequency (Fig. 1.3) [6]. This feature has been recently found in a Chinese edible frog [7], suggesting a possible common generation mechanism of IMDs in animals with distinct inner ear structures. This characteristic also implies that the dynamics of the inner ear cannot be accounted for by the response of a single nonlinear oscillator.

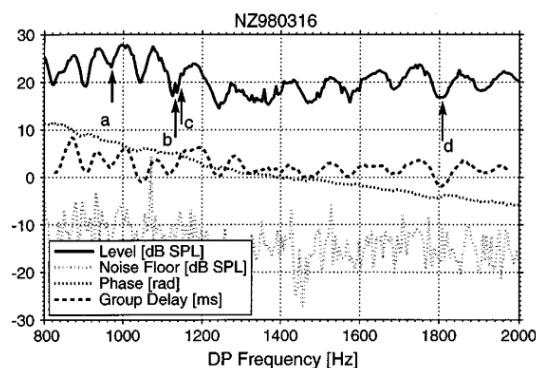


Figure 1.3 The amplitude of IMD recorded from a human subject.

At frequency $2f_1 - f_2$, the IMD amplitude displays a quasi-periodic variation with the distortion frequency (solid line) [6].

Hair cells of most vertebrate species are anchored to an overlying structure which provides a strong intercellular mechanical coupling. Hair cells are primarily organized in order of their natural frequencies, a feature termed tonotopic organization. We hypothesize that this cooperativity between hair cells may result in the quasi-periodic frequency dependence of the IMD amplitude. We have developed a phenomenological model based on a chain of coupled nonlinear oscillators to describe the generation of intermodulation distortions from the inner ear. Each oscillator is assumed to be in a vicinity of a supercritical Hopf bifurcation and possess a distinct characteristic frequency. The amplitude of the distortion signals will then be compared to the experimental results of IMDs from Chinese edible frog available in the literature to unravel the underlying mechanisms for the generation of the auditory distortions.

1.2 Objectives

1. To study the generation of intermodulation distortions from a chain of coupled nonlinear oscillators.
2. To compare the frequency dependence of the third-order distortion amplitudes from a chain of coupled nonlinear oscillators on the distortion signals generated by the inner ears of Chinese edible frogs.

1.3 Scope of this research

1. We will study intermodulation distortions from a single nonlinear oscillator, and a chain of nonlinear oscillators, each poised near a supercritical Hopf bifurcation. Only effects of mechanical coupling between nearest neighboring oscillators will be investigated.
2. Intermodulation distortions will be studied by performing numerical simulations using the 5th – order Runge-Kutta method.
3. Numerical results will be compared to previous experimental results from Chinese edible frogs.

1.4 Procedures

1.4.1 Literature review and define an objective of the study

Reviewing the books and previous publications related to the physiology of the inner ears of low vertebrate species such as lizards and frogs, the generation of DPOAEs, and the nonlinear dynamics. The assumption of the model are based on previous theoretical and experimental studies.

1.4.2 Create a mathematical model to describe the generation of DPOAEs

The mathematical model used in this study is based on the nonlinear dynamics. Each hair cell is modeled as a nonlinear oscillator poised near a supercritical Hopf bifurcation and coupled to its neighbors. The model is related to the physiology of the Chinese edible frog's inner ear in which all hair cells are commonly attached to an overlying membrane. The effects from driving forces with two frequencies will be investigated in a system of nonlinear oscillators arranged in order of their characteristic frequencies, or following a random order of characteristic frequencies.

1.4.3 Numerical simulations and analyses

The equations that describe the dynamics of the oscillators are solved by a numerical method. Numerical simulations are performed on MATLAB. The simulation results of the response from individual and all oscillators in the system will be

analyzed to find the mechanism behind the generation of a quasiperiodic behavior in the total IMD amplitude.

1.4.4 Comparison of the simulation results with the experimental results, conclusion of the study, and writing the thesis

Comparison between simulation and experimental results will be performed to examine the simulation results and determine the limitation of the model. After that, the results are summarized and concluded.

1.5 Expected outcome

We expect to develop a mathematical model for the generation of intermodulation distortions from the Chinese edible frog inner ears. The model will provide further insight into how the inner ear operates.

1.6 Overview

The next chapter consists of studies and theory about an auditory organ of frog, the otoacoustic emission, and Hopf bifurcation equation, which are involved in this study. Chapter 3 consists of the details about the derivation of the mathematical model used in this study, data analysis, and details about the parameters used in the mathematical model. Chapter 4 shows the simulation results from the mathematical model alongside the discussion and the comparison with the results from experiments. Lastly, the conclusion of this study is presented in chapter 5.

CHAPTER 2

THEORETICAL BACKGROUND AND LITERATURE REVIEWS

2.1 The physiology of the vertebrate inner ear

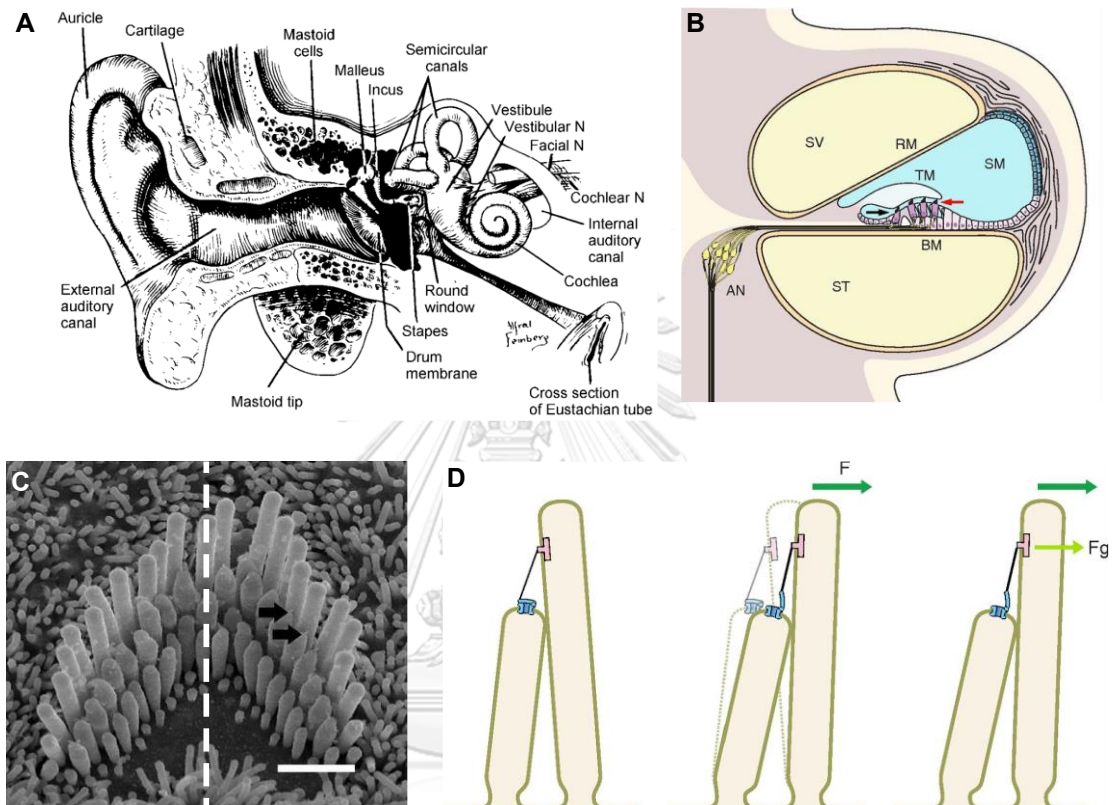


Figure 2.1 The physiology of the vertebrate ear and inner ear.

(A) A schematic drawing of the mammalian ear illustrates the outer, middle, and inner ear [8]. (B) A schematic drawing of the cross-section of the mammalian cochlea shows the organ of Corti situated atop the basilar membrane (BM) [3]. Hair cells are indicated by the red arrow. (C) An electron micrograph of a hair bundle from a rat cochlea (scale bar 1 μm) [3]. The dashed line indicates the direction of the bundle's deflection associated with the gating of mechanosensitive ion channels. (D) A schematic drawing of two adjacent stereocilia within a hair bundle. The movement of the bundle due to a driving force can open the ion channels [3].

In this section, we briefly describe the general structure of the vertebrate ears by focusing on those of mammals and amphibians. The ears of mammals consist of three parts: the outer, middle, and inner ear. The outer ear includes the ear lobe and the ear canal. The middle ear contains the eardrum and three ossicles: malleus, incus, and stapes. The inner ear of mammals constitutes the cochlea, and the semicircular canals.

On the other hand, the amphibian's ear lacks the outer ear, and their middle ear comprises of one ossicle. The inner ear consists of several auditory organs, two of which process signals within the acoustic frequency range, i.e., the amphibian papilla and basilar papilla. Further details on the structures of these two organs will be discussed in Section 2.2 as they are directly relevant to our mathematical model.

When a sound wave reaches the outer ear, it traverses the ear canal and impinges on the tympanic membrane in the middle ear. The resulting vibrations of the tympanic membrane will evoke the motion of the three middle-ear ossicles and subsequently transfer the acoustic energy into the cochlea via the oval window. The cochlea is a spiral-shaped organ comprising of three parallel tubes filled with fluid. The basilar membrane lies along the length of the middle tube, separating the tube into two compartments. Hair cells are embedded on the basilar membrane, arranged in arrays in order of their detection frequencies. When the sound wave reaches the inner ear, the difference in the fluid pressure across the basilar membrane generates the membrane's deflection, resulting in a transverse wave whose amplitude peaks at the location containing hair cells with the natural frequencies close to the signal frequency. However, this transverse wave with a sharp envelop has not been observed in other vertebrates including amphibians.

Hair cells are the biological acoustic sensors of the auditory system. The apical protrusions of each hair cell consist of a group of cilia, termed the hair-cell bundle. The deflection of the bundle evoked by an external force modulates the tension in the fiber connecting between adjacent cilia, resulting in the gating of the

mechano-sensitive ion-channels which elicits an influx of cations. This process alters the electric potential of the cell membrane, and subsequently initiates the release of neurotransmitters at the cell body.

Individual hair-cell bundles behave as highly nonlinear oscillators. Under a constant force, the displacement of the bundle depends nonlinearly on the force magnitude (Fig 2.2 A, solid line). This is associated with the reduction of the hair bundle's stiffness over a narrow range of the bundle's displacement. Under appropriate chemical conditions, the stiffness of the cilia can be negative (Fig 2.2 A, dashed line). This behavior leads to an instability of the hair-cell bundle, causing it to spontaneously oscillate in the absence of driving force.

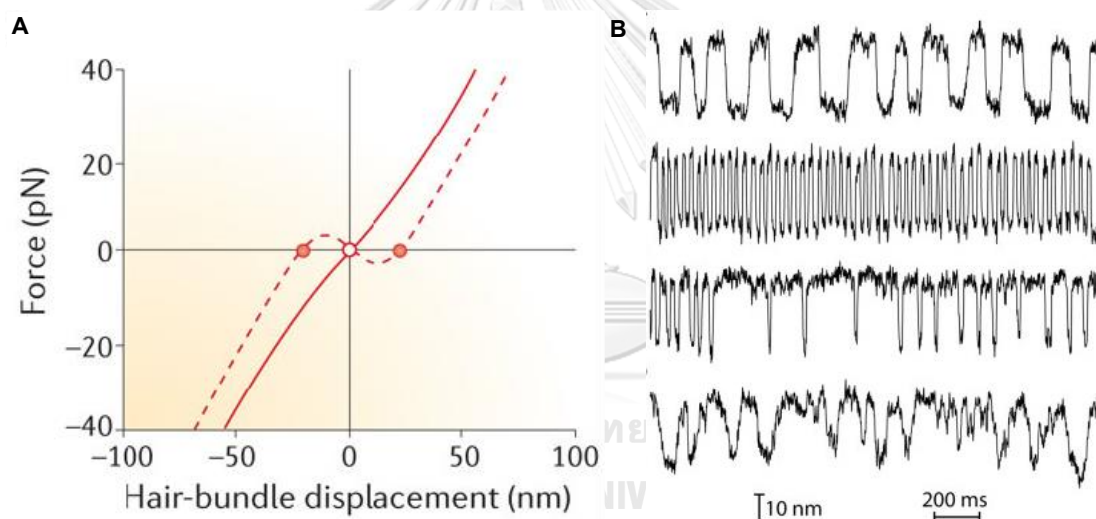


Figure 2.2 Response of a hair bundle with and without a driving force.

(A) Relation between force and displacement of a hair bundle. Solid and dashed lines indicate high and low calcium concentration, respectively [9]. (B) Displacement of Bullfrog's hair bundles without a driving force [10].

In response to a sinusoidal force, the amplitude of the bundle displacement exhibits a nonlinear dependence on the magnitude of the driving force, described by $R \propto F^{1/3}$ (Fig 2.3 A, red line). This feature can be beneficial to the auditory system as a mechanism which amplifies low-level inputs, as well as prevents damages caused

by loud sounds. Moreover, upon being driven by a force with 2 or more frequencies, the displacement of the hair bundle incorporates components at frequencies that are linear combinations of the frequencies of the applied force (Fig 2.3 B). This feature is associated with the intermodulation distortions, a common characteristic of a nonlinear system.

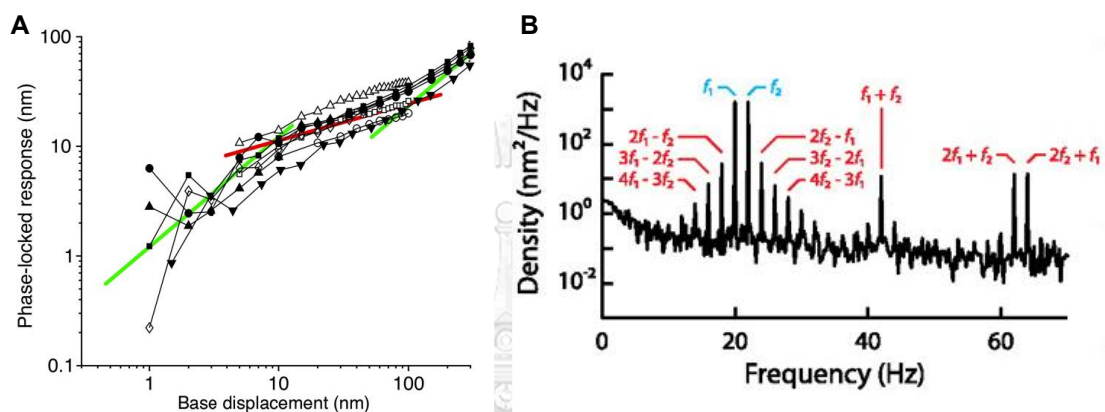


Figure 2.3 Nonlinear properties of a hair bundle.

(A) Nonlinear response from hair cell oscillation to stimulus force. At low driving force amplitude, the hair cell oscillates with an amplitude that shows an approximately linear dependence on the driving force (green line with slope=1). In contrast, over the range of moderate driving forces, the hair-bundle oscillation amplitude increased nonlinearly (red line with slope=0.3) [11]. (B) Frequencies spectrum from the response of an oscillator stimulated by two sinusoidal forces with equal amplitude (blue) shows peaks at frequencies that are linear combinations of the frequencies of the stimulus force (red) [5].

2.2 Anatomy of the frog's inner ear

Here, we describe the structures of the amphibian and basilar papillae, the two sensory organs within the frog's inner ear sensitive to acoustic inputs. These characteristics are common among amphibian species in the order Anuran, which includes all frog species. Hair cells in the amphibian papilla are arranged on a n elongated surface. Their detection frequencies increase linearly with distance

measured from an end of the papilla. In bullfrogs, the amphibian papilla hair cells process signals within the frequency range around 100 to 800 Hz [12].

For the basilar papilla, hair cells were arranged randomly on a small patch of epithelium lying on the inner surface of a ring-like shape, with the response frequency ranging from approximately 1000 to 1800 Hz [13]. In each organ, the tips of hair bundles are commonly attached to an overlying tectorial structure that can impose mechanical coupling between the bundles. Measurements from the basilar papilla reveal that the tectorial membrane vibrates as a rigid structure and deforms minimally in response to an incoming sound. This suggests that the tectorial structure has a high spring constant. Additionally, in contrast to the mammalian cochlea, lower vertebrate hair cells are embedded in a rigid cartilaginous base. Therefore, the amphibian inner ear lacks a flexible structure that can mediate a transverse wave. The acoustic energy provided by an incoming sound is thus presumably distributed equally to all hair cells in the sensory organ.

2.3 Otoacoustic emissions

The inner ear can actively produce acoustic energy, which can be measured in the ear canal as low-level sounds, termed otoacoustic emissions (OAEs). Typical measurements of OAEs are performed by inserting a sensitive microphone in the ear canal. OAEs have been recognized as a manifestation of the internal active processes and the nonlinearity of the inner ear. OAEs can be categorized into two types based on the stimulations [14]. First, spontaneous otoacoustic emissions (SOAEs) can be detected in the absence of acoustic stimulus. Second, evoked otoacoustic emissions (EOAEs) occur in response to sounds. EOAEs can be further classified based on the type of stimulations.

Under a stimulus of two frequencies, denoted by f_1 and f_2 , the inner ear produces low-level sounds at linear combinations of the stimulus frequencies such as $2f_1 \pm f_2$, $2f_2 \pm f_1$, $3f_1 \pm 2f_2$ and $3f_2 \pm 2f_1$. This type of EOAE measurable in the

ear canal is called distortion product otoacoustic emission (DPOAEs). This characteristic of the inner ear parallels the intermodulation distortions displayed by a nonlinear oscillator, as well as single hair bundles.

The generation mechanism of DPOAEs from the mammalian cochlea has been previously proposed [6, 15]. Upon stimulated by a two-frequency tone, groups of hair cells whose natural frequencies range between f_1 and f_2 will respond and generate IMDs. This distortion signal travels outward to the outer ear (1st DPOAE signal), as well as toward the end of the cochlea. This inwardly propagating signal will be amplified as it approached hair cells whose detection frequencies coincide with the distortion's. At a site of the basilar membrane that has an irregularity in its physical properties, this distortion is reflected outward to the outer ear (2nd DPOAE signal). Due to the phase difference between the two DPOAE signals, their interference can lead to a quasiperiodic variation in its intensity across the stimulus frequency. In human, this unique feature is called DPOAE fine structure. The local maxima (minima) corresponding to the constructive (destructive) interference of the two distortion signals. However, similar quasi-periodic patterns have been previously observed in the DPOAE level of Chinese edible frogs [16]. As the inner ear of amphibian lacks a flexible structure that can mediate a transverse wave, the aforementioned theory is not plausible to describe the quasi-periodic variation in the frog's DPOAE amplitude.

2.4 Derivation of a nonlinear oscillator displaying a supercritical Hopf bifurcation

A dynamical system operating near a supercritical Hopf bifurcation has been prevalently used to describe with the dynamics of individual hair-cell bundles [4, 5, 17]. In this section, we demonstrate that its mathematical formulation can be derived from a mechanical oscillator subject to a nonlinear spring or a nonlinear damping coefficient.

The derivation of the normal form of a supercritical Hopf bifurcation will follow [18]. For a weakly nonlinear oscillator with a characteristic frequency f_0 under a small perturbation, the equation of motion can be written as

$$\ddot{x} + 4\pi^2 f_0^2 x = f(x, \dot{x}) + F(t) \quad (2.1)$$

where $\dot{x} = \frac{dx}{dt}$, $\ddot{x} = \frac{d^2x}{dt^2}$ and $f(x, \dot{x})$ is a nonlinear function accounting for a nonlinear damping coefficient or the nonlinear part of the spring constant. The external force $F(t)$ is described by a periodic function $F(t) = F(t + T)$ at frequency $f = 1/T$. We assume that the solution of equation 2.1 can be written as

$$x(t) = \frac{1}{2} (A(t)e^{i2\pi ft} + A^*(t)e^{-i2\pi ft}), \quad (2.2)$$

where $A(t)$ is a time dependent complex amplitude. The observed frequency of $x(t)$ can deviate from f if the amplitude A rotates on the complex plane. However, we assume that $A(t)$ is changing on a timescale much longer than the period of the external force.

Equation 2.1 is rewritten as

$$\ddot{x} + 4\pi^2 f^2 x = (4\pi^2 f^2 - 4\pi^2 f_0^2)x + f(x, \dot{x}) + F(t), \quad (2.3)$$

and represented as a system of first-order differential equations,

$$\begin{aligned} \dot{x} &= y \\ \dot{y} &= -4\pi^2 f^2 x + (4\pi^2 f^2 - 4\pi^2 f_0^2)x + f(x, \dot{x}) + F(t). \end{aligned}$$

We can write $y(t)$ as

$$y(t) = \frac{1}{2} (i2\pi f A(t)e^{i2\pi ft} - i2\pi f A^*(t)e^{-i2\pi ft}), \quad (2.4)$$

assuming a small-time derivative of the complex amplitude $A(t)$. By substituting equations 2.2 and 2.4 into equation 2.3, we get

$$\dot{A} = \frac{e^{-i2\pi ft}}{i2\pi f} [(4\pi^2 f^2 - 4\pi^2 f_0^2)x + f(x, y) + F(t)]. \quad (2.5)$$

Under the assumption of a slowly varying complex amplitude. The right-hand side of equation 2.5 is small. We then apply the averaging method to this equation by assuming that the time derivative of time average of $A(t)$ is equal to the time average of time derivative, i.e.,

$$\frac{d}{dt} \left(\frac{1}{T} \int_0^T A(t) dt \right) = \frac{1}{T} \int_0^T \frac{dA(t)}{dt} dt = \langle \dot{A}(t) \rangle$$

where $\langle \dots \rangle$ denotes a time average,

$$\langle A(t) \rangle = \frac{1}{T} \int_0^T A(t) dt.$$

Thus, equation 2.5 can be simplified by averaging over a period of the driving force. First, averaging of the term $\frac{e^{-i2\pi ft}}{i2\pi f} (4\pi^2 f^2 - 4\pi^2 f_0^2)x$ gives

$$\begin{aligned} \frac{1}{T} \int_0^T \frac{e^{-i2\pi ft}}{i2\pi f} (4\pi^2 f^2 - 4\pi^2 f_0^2) x(t) dt &= \frac{1}{T} \int_0^T \frac{e^{-i2\pi ft}}{i2\pi f} (4\pi^2 f^2 - \\ &4\pi^2 f_0^2) \frac{1}{2} (A(t)e^{i2\pi ft} + A^*(t)e^{-i2\pi ft}) dt, \end{aligned}$$

which gives

$$\frac{1}{T} \int_0^T \frac{e^{-i2\pi ft}}{i2\pi f} (4\pi^2 f^2 - 4\pi^2 f_0^2) x(t) dt = -i \frac{4\pi^2 f^2 - 4\pi^2 f_0^2}{4\pi f} \langle A(t) \rangle.$$

Next, we average the term

$$\frac{e^{-i2\pi ft}}{i2\pi f} F(t)$$

where a periodic function $F(t)$ can be written as a Fourier series by

$$F(t) = \frac{a_0}{2} + \sum_{n=1}^{\infty} a_n \cos\left(\frac{2\pi nt}{T}\right) + b_n \sin\left(\frac{2\pi nt}{T}\right).$$

Averaging the term $\frac{e^{-i2\pi ft}}{i2\pi f} \varepsilon F(t)$ preserves only the first Fourier harmonic ($n = 1$) of the periodic function $F(t)$,

$$\frac{1}{T} \int_0^T \frac{e^{-i2\pi ft}}{i2\pi f} F(t) dt = \frac{1}{T} \int_0^T \frac{e^{-i2\pi ft}}{i2\pi f} \left(a_1 \cos\left(\frac{2\pi t}{T}\right) + b_1 \sin\left(\frac{2\pi t}{T}\right) \right) dt,$$

which gives a complex constant $-iF_0$ where F_0 denotes a constant proportional to the amplitude of the first Fourier harmonic of the periodic function $F(t)$. Next, we determine the average of the term

$$\frac{e^{-i2\pi ft}}{i2\pi f} f(x, y).$$

If we assume that $f(x, y)$ is polynomial in x and y , it can be written as a polynomial of $A(t)e^{i2\pi ft}$ and $A^*(t)e^{-i2\pi ft}$. Then we can write the term as

$$\begin{aligned} f(x, y) &= \sum_{p=0}^{\infty} \sum_{q=0}^{\infty} \left(\frac{1}{2} (A(t)e^{i2\pi ft} + A^*(t)e^{-i2\pi ft}) \right)^p (i\pi f A(t)e^{i2\pi ft} - \\ &i\pi f A^*(t)e^{-i2\pi ft})^q, \end{aligned}$$

which can be expanded as

$$\sum_{p=0}^{\infty} \sum_{q=0}^{\infty} \sum_{r=0}^p \sum_{s=0}^q \left(\frac{A(t)e^{i2\pi ft}}{2} \right)^{p-r} \left(\frac{A^*(t)e^{-i2\pi ft}}{2} \right)^r (i\pi f A(t)e^{i2\pi ft})^{q-s} (-i\pi f A^*(t)e^{-i2\pi ft})^s.$$

The combination of the polynomials in $f(x, y)$ can be simplified to a polynomial function of $A(t)e^{i2\pi ft}$ and $A^*(t)e^{-i2\pi ft}$ as

$$f(x, y) = \sum_{n=0}^{\infty} \sum_{m=0}^{\infty} a_{nm} (A(t)e^{i2\pi ft})^n (A^*(t)e^{-i2\pi ft})^m.$$

Averaging the term $\frac{e^{-i2\pi ft}}{i2\pi f} f(x, y)$ can be written as

$$\begin{aligned} & \frac{1}{T} \int_0^T \frac{e^{-i2\pi ft}}{i2\pi f} f(x, y) dt = \\ & \frac{1}{T} \int_0^T \frac{e^{-i2\pi ft}}{i2\pi f} \sum_{n=0}^{\infty} \sum_{m=0}^{\infty} a_{nm} (A(t)e^{i2\pi ft})^n (A^*(t)e^{-i2\pi ft})^m dt, \end{aligned}$$

which gives

$$\frac{1}{T} \int_0^T \frac{e^{-i2\pi ft}}{i2\pi f} f(x, y) dt = \frac{1}{i2\pi f T} \sum_{n=0}^{\infty} \sum_{m=0}^{\infty} a_{nm} \int_0^T \langle A \rangle^n \langle A^* \rangle^m e^{i2\pi ft(n-m-1)} dt.$$

For a slowly varying complex amplitude, the integral is non-zero if $n - m - 1 = 0$. Thus, averaging the term $\frac{e^{-i2\pi ft}}{i2\pi f} f(x, y)$ can be written as

$$\frac{1}{T} \int_0^T \frac{e^{-i2\pi ft}}{i2\pi f} f(x, y) dt = \frac{1}{2\pi i} \sum_{m=0}^{\infty} a_{nm} \int_0^T (|A|^2)^m A dt,$$

where the solution with the possible lowest-order nonlinear term should have the form $\langle |A|^2 A \rangle$. Then, for small amplitude of oscillation, we keep only the linear and the first nonlinear terms. Then we obtain

$$\frac{1}{T} \int_0^T \frac{e^{-i2\pi ft}}{i2\pi f} f(x, y) dt \approx \mu \langle A(t) \rangle - (\gamma + i\kappa) \langle |A(t)|^2 A(t) \rangle$$

where the coefficient of the imaginary part of the linear term is absorbed into the first term on the right-hand side of equation 2.5. The coefficient of the real part of the linear term is denoted as μ . The parameters γ and κ represent the coefficients of the nonlinear term. All coefficients are determined by the specific form of $f(x, y)$.

After averaging all terms from the right-hand side of equation 2.5, the complex amplitude, $\langle A(t) \rangle$, obeys the normal form of a system near a supercritical Hopf bifurcation point under a driving force.

$$\langle \dot{A}(t) \rangle = \left(\mu - i \frac{4\pi^2 f^2 - 4\pi^2 f_0^2}{4\pi f} \right) \langle A(t) \rangle - (\gamma + i\kappa) \langle |A(t)|^2 A(t) \rangle - iF_0 \quad (2.6)$$

where the parameter μ serves as the order parameter of the system. The parameter κ describes the nonlinear dependence of the oscillation frequency on the amplitude

which can be negative, positive or zero. For a small frequency detuning $\delta f = f - f_0$ with $\delta f \ll f_0$, one can show that $\nu = \frac{4\pi^2 f^2 - 4\pi^2 f_0^2}{4\pi f} = \pi \frac{f^2 - f_0^2}{f} = \pi f \left[1 - \left(\frac{\delta f}{f} \right)^2 \right] \approx 2\pi \delta f = 2\pi(f - f_0)$. Equation 2.6 can be rewritten as

$$\langle \dot{A}(t) \rangle = (\mu - i\nu)\langle A(t) \rangle - (\gamma + i\kappa)\langle |A(t)|^2 A(t) \rangle - iF_0. \quad (2.7)$$

As mentioned earlier that $\langle A(t) \rangle$ is a time dependent complex amplitude. To obtain the displacement of oscillator, we assume that the system can be described by a complex dynamical variable, $Z(t)$, defined as $Z(t) = \langle A(t) \rangle e^{i2\pi f t}$. Note that from equation 2.2, the displacement of the oscillator is the real part of the complex variable, $x(t) = \text{Re}(Z(t))$. By putting $Z(t) = \langle A(t) \rangle e^{i2\pi f t}$ into equation 2.7, we get

$$\dot{Z} = (\mu + i2\pi f_0)Z - (\gamma + i\kappa)|Z|^2 Z - iF_0 e^{i2\pi f t}. \quad (2.8)$$

2.5 Verification of supercritical Hopf bifurcation

In this section, we demonstrate that the simplified form of equation 2.8 in the absent of a driving force can display a supercritical Hopf bifurcation. We describe the definition of a supercritical Hopf bifurcation based on [19].

For simplicity, we set the parameter γ to one and κ to zero, equation 2.8 can be rewritten as

$$\dot{Z} = (\mu + i2\pi f_0)Z - |Z|^2 Z. \quad (2.9)$$

We can write as $Z(t) = v(t) + iw(t)$ and equation 2.9 become

$$\dot{v} + i\dot{w} = (\mu + i2\pi f_0)(v + iw) - (v^2 + w^2)(v + iw),$$

which can be separated into the real and imaginary parts as

$$\begin{aligned} \dot{v} &= \mu v - 2\pi f_0 w + \mathcal{O}(v^3) + \mathcal{O}(w^3) \\ \dot{w} &= \mu w + 2\pi f_0 v + \mathcal{O}(v^3) + \mathcal{O}(w^3). \end{aligned}$$

This system displays a fixed point at the origin. For small displacements, near the fixed point, we can write the Jacobian matrix from these two equations to determine how the eigenvalues behave during the bifurcation. So, the Jacobian is

$$J = \begin{pmatrix} \mu & -2\pi f_0 \\ 2\pi f_0 & \mu \end{pmatrix},$$

which has eigenvalues $\lambda = \mu \pm i2\pi f_0$. This linear stability analysis assumes that time dependence of the dynamical variables are of the form $e^{\lambda t}$.

The eigenvalues suggest that the dynamical variables v and w decay exponentially for negative μ . Therefore, the fixed point at the origin is stable for this range of control parameter. On the other hand, when μ is positive, the dynamical variables diverge from the origin, indicating that the fixed point becomes unstable. The system shows a periodic solution at frequency f_0 , which appears as a limit cycle in the phase space. Thus, the stability of the system changes from a stable fixed point to a stable limit cycle when μ increases from negative to positive values and a supercritical Hopf bifurcation occurs at $\mu = 0$.

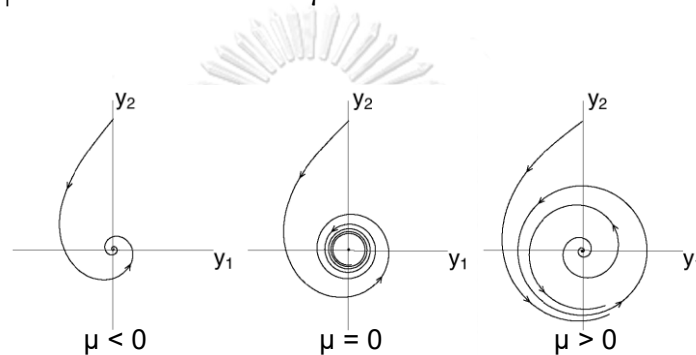


Figure 2.4 Diagram of a supercritical Hopf bifurcation of two-dimensional case [20].

2.4 Mathematical model of the inner ear based on nonlinear oscillators

In this section, we describe a mathematical model previously developed to represent the simple inner ear, such as those of lower vertebrates, in which the transverse wave on the basilar membrane is not likely to occur. The model is based on the experimental studies that the dynamics of each hair-cell bundle are well consistent with a nonlinear oscillator poised near a supercritical Hopf bifurcation. The inner ear is then regarded as a chain of coupled oscillators, arranged in order of their characteristic frequencies. This model has been originally developed to describe to generation of SOAEs from the inner ear [21-23]. The results from the model indicate that the strength of coupling controls the behavior of the oscillators. Under an appropriate coupling strength, the spontaneous motions of oscillators were synchronized into clusters, each oscillating at a distinct frequency. The associated

spectrum of the system's total displacement displays several peaks. This agrees with SOAE spectra observed in several species including humans and lizards.

In details, the mathematical model used in Vilfan et al. [21] and Wit et al. [22] works is obtained from an equation of motion of coupled oscillators, each subject to a negative damping. Upon reassigning the parameters and the dynamical variables, the normal form of coupled nonlinear oscillators near a Hopf bifurcation is obtained. To investigate the response to external tones, a sinusoidal function whose amplitude contains only the real part is added.

Another related model has been presented by Fruth et al. [24]. Similar to [21], the dynamics of an oscillator was described by a system of coupled generalized complex Ginzburg-Landau equation, with the coupling term represented by a pressure due to the fluid within the cochlea chamber. The main difference between this model and that presented in [21] is the driving force term. While Vilfan's contains only the real part, the force term in Fruth's model is purely imaginary. However, the results from both models were similar and agree with the main features of SOAEs.

As we have shown in section 2.2, the driving force term that does not depend on the displacement or velocity of the system will appear in the equation governing the dynamics of the dynamical variable as an imaginary part. In the next chapter, we will demonstrate that the force terms that depend on the oscillator's velocity will appear as a real part, and the force governed by the oscillator's displacement is purely imaginary.

CHAPTER 3

METHODS

3.1 Derivation of a chain of coupled Hopf oscillators equation

In the previous chapter, we have demonstrated that the dynamics of a mechanical oscillator subject to a nonlinear spring or damping coefficient can be described by a nonlinear dynamical system poised near a supercritical Hopf bifurcation. In this section, we show that a chain of mechanical oscillators coupled to their nearest neighbors with reactive coupling can be described by an array of coupled Hopf oscillators.

The equation of motion for the j^{th} oscillator can be represented as

$$\ddot{x}_j + 4\pi^2 f_{0j}^2 x_j = f(x_j, \dot{x}_j) + D_j(x_{j+1} + x_{j-1} - 2x_j) + B_j(\dot{x}_{j+1} + \dot{x}_{j-1} - 2\dot{x}_j) + F(t). \quad (3.1)$$

By using the method of averaging with solutions

$$x_j(t) = \frac{1}{2}(A_j(t)e^{i2\pi ft} + A_j^*(t)e^{-i2\pi ft})$$

$$y_j(t) = \frac{1}{2}(i2\pi f A_j(t)e^{i2\pi ft} - i2\pi f A_j^*(t)e^{-i2\pi ft}),$$

we obtain

$$\langle \dot{A}_j(t) \rangle + \left(\frac{4\pi^2 f_{0j}^2}{i2\pi f} - \frac{4\pi^2 f^2}{i2\pi f} \right) \langle A_j(t) \rangle = \frac{e^{-i2\pi ft} f(x_j, y_j)}{i2\pi f} + \left(\frac{D_j}{i2\pi f} + B_j \right) (\langle A_{j+1}(t) \rangle + \langle A_{j-1}(t) \rangle - 2\langle A_j(t) \rangle) - iF_0.$$

One can show that

$$\langle \dot{A}_j(t) \rangle = (\mu_j - i\Delta_j) \langle A_j(t) \rangle - (\gamma_j + i\kappa_j) \langle |A_j(t)|^2 A_j(t) \rangle + (\beta_j + i\delta_j) (\langle A_{j+1}(t) \rangle + \langle A_{j-1}(t) \rangle - 2\langle A_j(t) \rangle) - iF_0 \quad (3.2)$$

where $\Delta_j = 2\pi(f_{0j} - f)$ is the frequency detuning and β_j, δ_j are coupling parameters proportional to the coupling constant B_j, D_j in equation 3.1 where $\delta_j = \frac{-D_j}{2\pi f}$.

Again, for simplicity, we set the parameter γ_j to one and κ_j to zero. We define a complex dynamical variable $Z_j(t) = \langle A_j(t) \rangle e^{i2\pi ft}$ describing the displacement of the j^{th} oscillator. Equation 3.2 can be rewritten as

$$\dot{Z}_j = (\mu_j + i2\pi f_{0j})Z_j - |Z_j|^2 Z_j + (\beta_j + i\delta_j)(Z_{j+1} + Z_{j-1} - 2Z_j) - iF_0 e^{-i2\pi f t} \quad (3.3)$$

3.2 A model of a chain of coupled nonlinear oscillators

We utilize a mathematical model previously developed to represent the system of hair cells within the simple inner ear. Each hair bundle was represented by a nonlinear oscillator poised near a supercritical Hopf bifurcation [21]. *In vivo* hair bundles in the papilla were commonly attached to the tectorial membrane, which provided a mechanical connection between the bundles. This coupling was modeled as a viscoelastic material joining the adjacent oscillators.

From equation 3.3, we assume that the coupling parameter β_j and δ_j are constant, rewritten as d_R and d_I , respectively. From the definition, $\delta_j = \frac{-D_j}{2\pi f}$, the value of d_I is negative.

The structure of the amphibian inner ear suggests that all hair bundles are commonly driven by the overlying tectorial structure. We simplify the distribution of acoustic energy to hair bundles by assuming that all oscillators are driven by identical forces each comprising of two sinusoidal functions. We have shown that, a real, periodic force applied to a nonlinear mechanical oscillator is of the form $iF_0 e^{-i2\pi f t}$ in the equation governing the complex dynamical variable $Z(t)$. However, in our simulations, we choose a purely imaginary force term of the form $+iF_0 \cos(2\pi f t)$. This reflects the means of hair bundle stimulation, which occurs via an elastic element connecting each bundle to the tectorial membrane. However, this form of force term in fact includes the relative displacement between the oscillators and their overlying structure. We have added a comment on this in the section 4.6. In addition, the sign of the force term represents the initial phase of the waveform, and thus should not affect our analysis of the oscillators' amplitudes nor their relative phase of the response. The equation of N active coupled oscillators with driving force can be represented as

$$\dot{Z}_j = (\mu_j + i2\pi f_{0j})Z_j - |Z_j|^2 Z_j + (d_R + id_I)(Z_{j+1} + Z_{j-1} - 2Z_j) + \quad (3.4)$$

$$iF_1 \cos(2\pi f_1 t) + iF_2 \cos(2\pi f_2 t).$$

To account for the free ends of the chain, the coupling term is replaced by $(d_R + id_I)(Z_2 - Z_1)$ for the first oscillator, $j = 1$, and by $(d_R + id_I)(Z_{N-1} - Z_N)$ for the last oscillator in the chain, $j = N$. The displacement of j^{th} oscillator is $x_j = \text{Re}(Z_j)$. Each oscillator displays a supercritical Hopf bifurcation when $\mu_j = 0$, f_{0j} is the characteristic frequency of j^{th} oscillator, d_R is dissipative coupling coefficient, and d_I is reactive coupling coefficient. The fourth and fifth terms on the right-hand side of the equation represent driving force which applied to an oscillator where F_1 and F_2 are the amplitudes of the driving force at frequencies f_1 and f_2 , respectively.

3.3 Data analysis

All simulations and analyses were performed in MATLAB (2019b). Numerical simulations of equation 3.4 were performed by 5th-order Runge-Kutta method to improve the accuracy of the simulations, at a time step of 0.001 s. Each simulation was performed for 150 seconds. The trace during the first 50 seconds was excluded from further analyses to avoid any transient response. The finite-time Fourier transform was performed on each oscillator's displacement to obtain its amplitude spectrum. The IMD amplitudes of the j^{th} oscillator defined by $|\tilde{x}_j(f_{IMD})|$ were obtained from the magnitude of its complex Fourier component, $\tilde{x}_j(f)$, of the oscillator's displacement, $x_j(t)$.

We assumed that the total IMD produced by the system was equal to a superposition of the distortion signals exhibited by each oscillator. The total IMD amplitude, denoted by $|\tilde{X}(f_{IMD})|$, was obtained from the magnitude of the linear sum of the distortion signals from all oscillators in the system, given by $\tilde{X}(f_{IMD}) = \sum_{j=1}^N \tilde{x}_j(f_{IMD})$.

The phase of the distortion signal from an oscillator was defined relative to the phase of the first oscillator in the chain, and can be calculated using the relation $\varphi_{j,1} \equiv \tan^{-1}(\text{Im}(\tilde{x}_{j,1})/\text{Re}(\tilde{x}_{j,1})) + (\pi/2)\text{sign}(\text{Im}(\tilde{x}_{j,1}))(1 - \text{sign}(\text{Re}(\tilde{x}_{j,1})))$ where $\tilde{x}_{j,1}(f_{IMD}) = \tilde{x}_j(f_{IMD})/\tilde{x}_1(f_{IMD})$.

3.4 Parameters selection

The values of the parameters in the model are estimated from physiological recordings of hair cells from the amphibian papilla of Bullfrog's inner ears. Hair cells in the amphibian papilla are sensitive to acoustic signals within the frequency range 200 Hz to 800 Hz [12]. After scaling by 200 Hz, we fixed the characteristic frequencies of the oscillators within a range between 1 and 4.

The number of hair cells, N , used in a previous study of the tokay gecko's inner ear was 80 [21]. As the length of the frog's amphibian papilla is approximately 2/3 of the size of the gecko's inner ear, we adjusted the number of oscillators to 60.

Hair bundles are tightly attached to the tectorial membrane, whose physical properties suggest that coupling between neighboring hair bundles should be dominated by the stiffness of the membrane and minimally contributed by the viscous drag between bundles [13]. The values of d_I used in this work are thus significantly higher than, d_R , which is fixed at zero [21, 23]. The strength of reactive coupling d_I will be varied as a free parameter in the model

CHAPTER 4

RESULTS AND DISCUSSION

4.1 Response from a single Hopf oscillator

Each hair bundle of the Bullfrog's inner ear was modeled as an active nonlinear oscillator which displayed a supercritical Hopf bifurcation. Our results from numerical simulations of a single oscillator were consistent with analytical calculations (Appendix A) and previous investigations [4, 11].

Upon being driven by a single sinusoidal force, the oscillator's response at the driving frequency, f , had the highest amplitude when f was closed to the oscillator's characteristic frequency, f_0 (Fig. 4.1 A). Moreover, by varying the driving force magnitude between 0.001 and 300, the response amplitude showed a compressive growth with the exponent of 0.33 (Fig. 4.1 B). These characteristics were consistent with analytical calculations of a driven oscillator near a supercritical Hopf bifurcation (Appendix A).

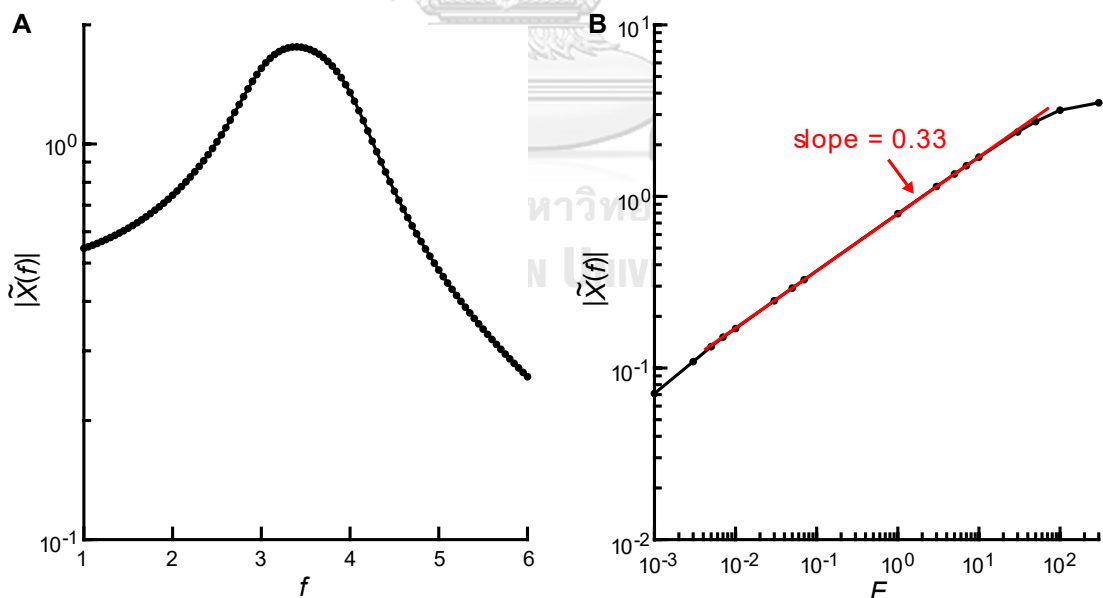


Figure 4.1 Response amplitude and compressive nonlinearity from a single oscillator.

(A) The response amplitude from a single oscillator as a function of driving frequency, f , varied from 1 to 6 with $f_0 = 3.5$ and $F = 11$. (B) A compressive

nonlinearity (red line) is observed in the response amplitude over the range of driving force $F = 0.01 - 70$.

Next, we applied two driving forces at different frequencies, with $f_2 = f_1 + 0.6$. Both components had an equal amplitude at $F = 11$. The oscillator's displacement displayed its intermodulation distortions (IMDs) at linear combinations of f_1 and f_2 (Fig. 4.2 A). The amplitude of the oscillator's displacement at frequency $2f_1 - f_2$ showed a similar behavior to the response to a single force, for which the response amplitude reached its highest value when $2f_1 - f_2$ is close to f_0 (Fig. 4.2 B). This feature was consistent with results from a previous theoretical study [4], and our analytical calculation (Appendix A).

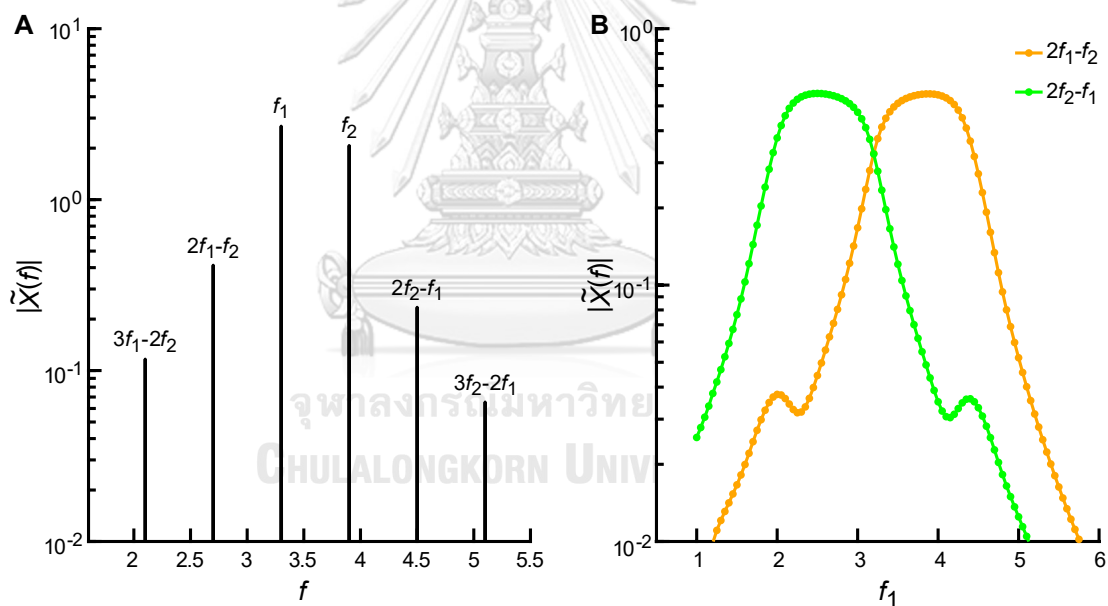


Figure 4.2 Effect of driving forces on a single oscillator.

(A) Frequency spectrum of a single oscillator with $f_0 = 3.5$ driven by driving forces with $f_1 = 3.3$ and $f_2 = 3.9$. (B) IMD amplitude at $2f_1 - f_2$ (orange) and $2f_2 - f_1$ (green) from a single oscillator driven by the driving frequency, f_1 , from 1 to 6. (A) and (B) using $F = 11$.

4.2 Determination of critical control parameter of a chain of coupled Hopf oscillators

We determined the value of the critical control parameter, μ_c , of a chain of oscillators, arranged in order of their characteristic frequencies by performing numerical simulations of the system's autonomous displacement. We defined the critical control parameter as the lowest control parameter at which at least one oscillator in the chain could undergo a sustained limit-cycle oscillation.

First, we determined the critical control parameter of each oscillator, μ_j , in a chain of coupled 60 oscillators arranged in order of their characteristic frequencies, f_0 , uniformly distributed from 1 to 4. The parameter μ was increased from -0.02 to 0.06, at a 0.001 increment. The initial displacement of each oscillator was fixed at a small, real value, 0.0001. The displacement of each oscillator was extracted from $Re(Z_j)$ (Fig. 4.3 A and B). As μ approached μ_j , the timescale at which the solution reached a steady state became increasingly slow. Instead of determining the amplitude of the steady oscillation, we divided the time trace into sections, each of 20 seconds long. After that, the root mean square of the displacement was calculated from each section.

When $\mu < \mu_j$, the oscillation decayed towards zero and the rms displacement decreased with time, following an exponential decay (Fig. 4.3 A and C). On the other hand, when $\mu > \mu_j$, the oscillation amplitude as well as the rms displacement increased with time (Fig. 4.3 B and D), displaying an exponential growth. We extracted the time constant of the exponential growth and decay by performing a linear fit to the rms displacement in a semi-log scale (Fig. 4.3 C and D). The slope of the linear function is positive for an exponential growth, and negative for an exponential decay.

The slope obtained from the linear fit to the rms displacement in a semi-log scale had an interpretation resembling that of the Lyapunov exponent, which determined the time evolution of the separation between two arbitrary points in a phase space. A positive Lyapunov exponent corresponded to the separation that increased exponentially with time, whereas a negative exponent indicated that the two points converged with their separation decayed exponentially. In our case, the time constant obtained from the fit of the rms displacement indicated the separation

between a point at the origin (0,0) and a point at our initial position (0.0001,0). A negative slope from the linear fit corresponded to a negative Lyapunov exponent, indicating that the system converged to the origin. On the other hand, a positive slope was analogous to a positive Lyapunov exponent. This suggested that the system's trajectory diverged from the origin, heading towards a stable limit cycle.

When plotted against μ , the time constant crossed zero at the value of μ_j (Fig. 4.3 E). We found that the value of μ_j remained closed to zero for all oscillators, within the resolution of μ employed in our analysis, 0.001 (Fig. 4.3 F). μ_c of the chain was then determined from the lowest μ_j (Fig. 4.3 G).

Upon varying the coupling constant d_I between -100 to 0, the result showed that μ_c remained close to zero over the range of d_I investigated. If we consider the order of magnitude of μ in the relation of slope and μ from Fig. 4.3 E, we can see that some oscillators' μ_j were of the order 10^{-3} , which remained very close to zero. This suggested that by setting $\mu = 0$, our system was poised very close to a critical point, and thus our choice for further simulations.

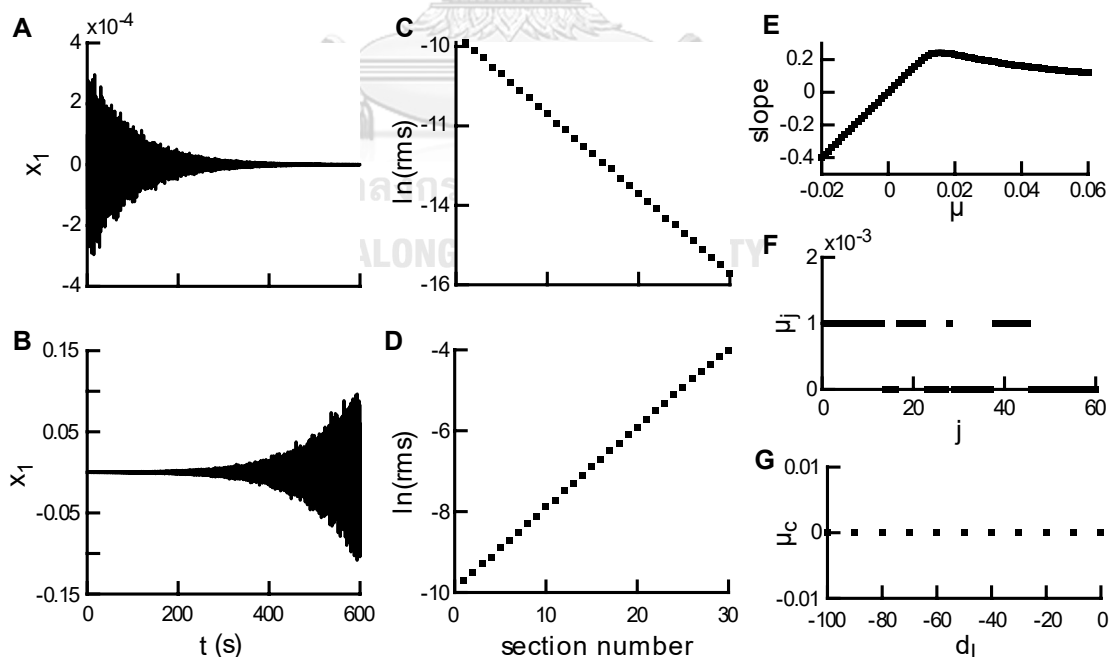


Figure 4.3 Determination of critical control parameter.

Displacement of an oscillator as a function of time from the first oscillator in the chain with $\mu =$ (A) -0.01 and (B) 0.01. The rms of the oscillator's displacement as a

function of section number with $\mu = (C) -0.01$ and (D) 0.01 . (E) The slope of the first oscillator's rms displacement as a function of parameter μ . (F) The magnitude of μ_j from each oscillator at $d_1 = -60$. (G) The magnitude of μ_c as a function of d_1 from -100 to 0 .

4.3 The total IMDs from a chain of uncoupled Hopf oscillators

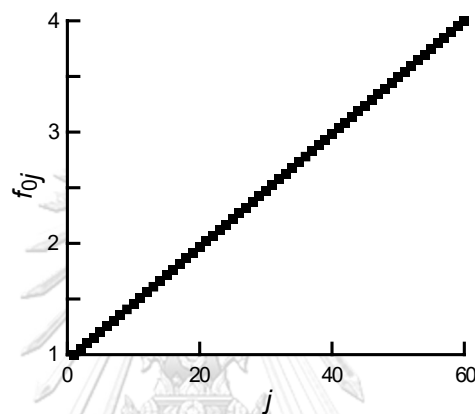


Figure 4.4 Characteristic frequency of each oscillator. f_0 , of j^{th} oscillator used to obtain results in Fig. 4.5 to 4.13.

A chain of 60 Hopf oscillators, arranged in an order of characteristic frequencies (Fig. 4.4) was used to investigate the effects of coupling on the IMD response. We fixed the difference between the two driving forces frequency, $df = f_2 - f_1$, at 0.6 . The driving frequency, f_1 , was varied from 0.6 to 5.0 at a step of 0.05 . From this section on, the driving force term was purely imaginary (Eq. 3.4).

In the absence of coupling, the simulation results showed that, at a weak driving force level, $F = 2$, the amplitude of the total IMD at frequency $2f_1 - f_2$ varied across driving frequencies with two peaks located at the stimulus frequency $f_1 = 1.0$ and 4.1 . When the driving force level was increased, $F = 6$, the level of the total IMD was enhanced and showed two peaks at $f_1 = 1.2$ and 4.2 with a single at $f_1 = 3.55$. An increase in F to 11 led to an absence of a local minimum, with the two peaks shifted slightly towards higher frequencies, $f_1 = 1.4$ and 4.3 . When F was increased to 15 and 25 , the total IMD profiles were enhanced and became nearly

flat. Two peaks could be observed at f_1 near the minimal and maximal characteristic frequencies (Fig. 4.5 A).

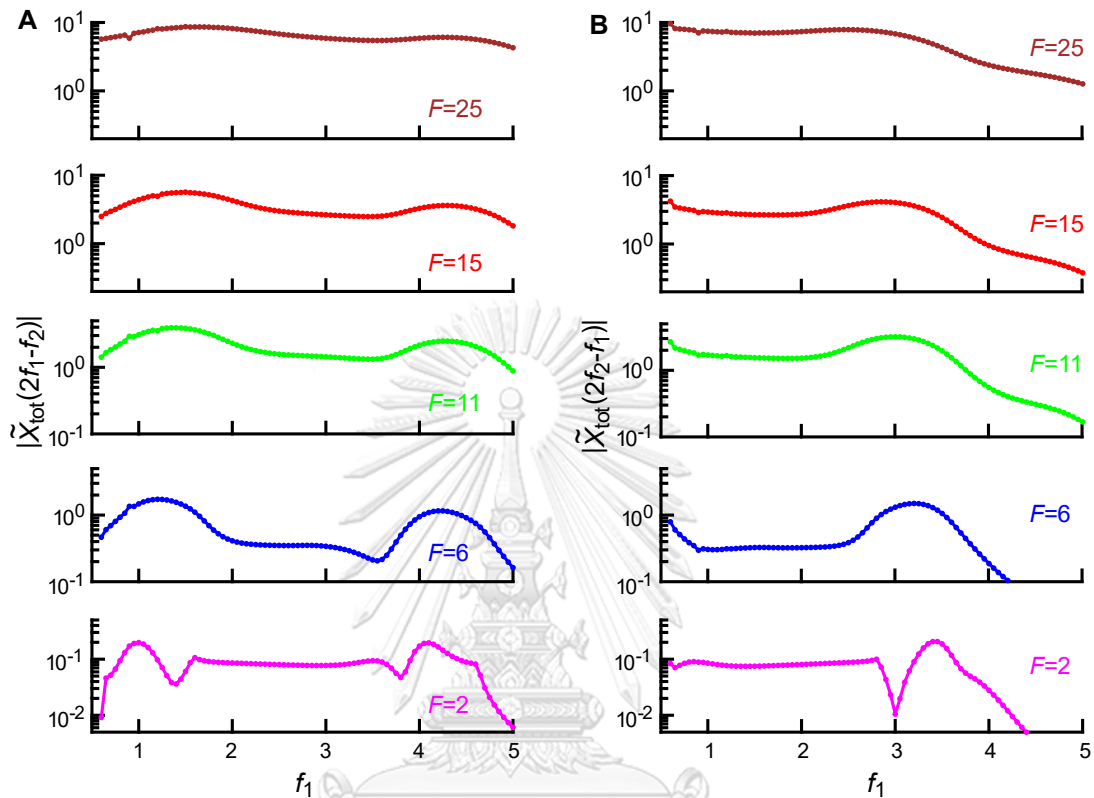


Figure 4.5 Amplitude of the total IMD from a system of uncoupled oscillators driven by the driving frequency, f_1 , from 0.6 to 5 at (A) $2f_1 - f_2$ and (B) $2f_2 - f_1$. $F = 2$ (magenta), 6 (blue), 11 (green), 15 (red), and 25 (brown).

On the other hand, the amplitude of total IMDs at frequency $2f_2 - f_1$ showed a single peak over the range of driving force level investigated. The peak was observed at f_1 near the maximal characteristic frequency. The peak frequency decreased as the forcing amplitude increased, from $f_1 = 3.4$ at $F = 2$, to $f_1 \sim 2.4$ at $F = 25$ (Fig. 4.5 B). In addition, the amplitude of the total IMD were enhanced when the level of driving force was increased.

To understand the details of the IMD amplitude variation, the amplitude of IMDs at frequency $2f_1 - f_2$ from each oscillator was investigated. To elucidate the response from each oscillator, the amplitude and the relative phase of IMDs at

frequency $2f_1 - f_2$ from each oscillator was plotted against its characteristic frequency. We noted that the relative phase of j^{th} oscillator's distortion was calculated relative to the phase of 1st oscillator's distortion. At a weak driving force level, $F = 2$, the amplitude of IMD showed two peaks at the oscillators whose f_0 were near f_1 and $2f_1 - f_2$ (Fig. 4.6 A). When the driving force level was increased to $F = 6$, the IMD amplitude showed a single broad peak at a higher amplitude level compared to the response to a weak driving force (Fig. 4.6 B). The relative phase increased smoothly with f_0 and spanned over a range of 2π . This resulted in a phase cancellation of the IMDs from individual oscillators. The relative phase behavior also corresponded to a travelling wave that propagated toward the oscillators which had lower characteristic frequencies (Fig. 4.6 A and B).

Upon varying the driving frequencies, the profile of the IMDs amplitude and relative phase remained unchanged with the peaks shifting toward the oscillators that had f_0 equal to f_1 and $2f_1 - f_2$. The IMDs amplitude and relative phase at frequency $2f_2 - f_1$ also showed similar behavior as $2f_1 - f_2$ with the peaks of IMDs amplitude occurring at f_0 near f_2 and $2f_2 - f_1$ (Fig. 4.6 C and D).

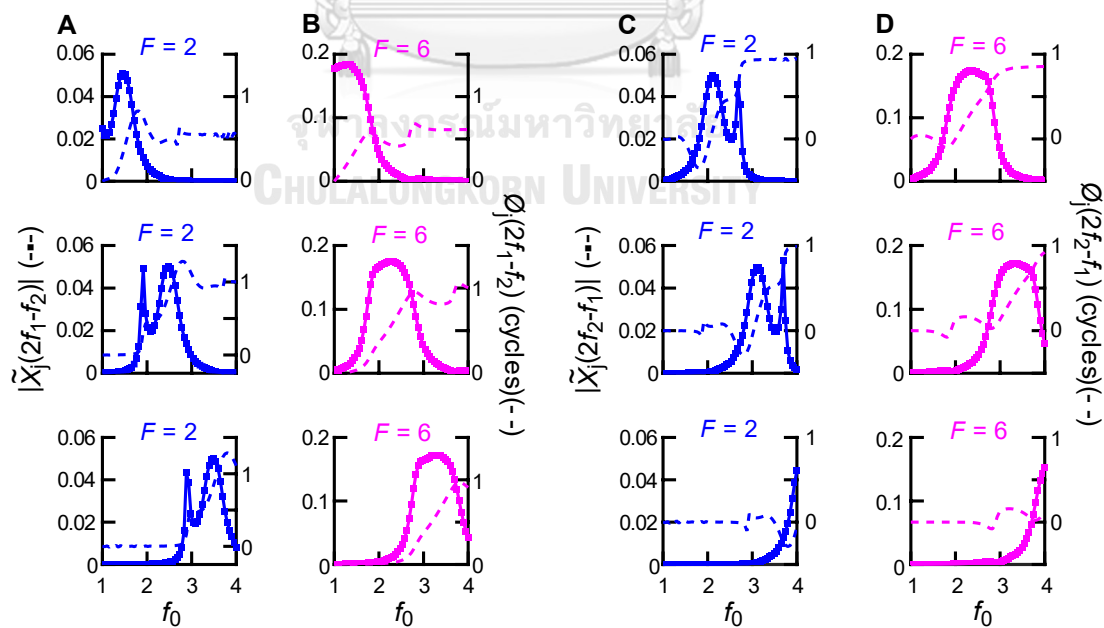


Figure 4.6 Oscillator's response from a system of uncoupled oscillators.

Individual distortion amplitude (squares) and relative phase (dash lines) at (A,B) $2f_1 - f_2$ and (C,D) $2f_2 - f_1$ with $F = 2$ (blue) and 6 (magenta). In each panel, from top to bottom, $f_1 = 1.5, 2.5,$ and 3.5 .

To illustrate how individual IMDs shaped the profile of the total IMD amplitude, individual IMDs were plotted in a polar coordinate (Fig. 4.7 A). The total IMD was represented as a vector, resulting from the vector sum of individual IMDs (Fig. 4.7 B).

The individual IMD polar plot rotated when the driving frequencies were varied. This resulted in the nearly flat total IMD amplitude over a broad range of stimulus frequencies. However, when the driving frequency, f_1 , was closer to $f_{0,1}$ or $f_{0,N}$, the narrower range of IMD phase distribution led to a stronger IMD amplitude because of an incomplete phase cancellation (Fig. 4.7 B). In contrast, when the driving frequency, f_1 , moved away from $f_{0,1}$ or $f_{0,N}$, the distribution of IMDs phase got wider which caused a more complete destructive interference between individual IMDs. This resulted in a weaker total IMD amplitude.

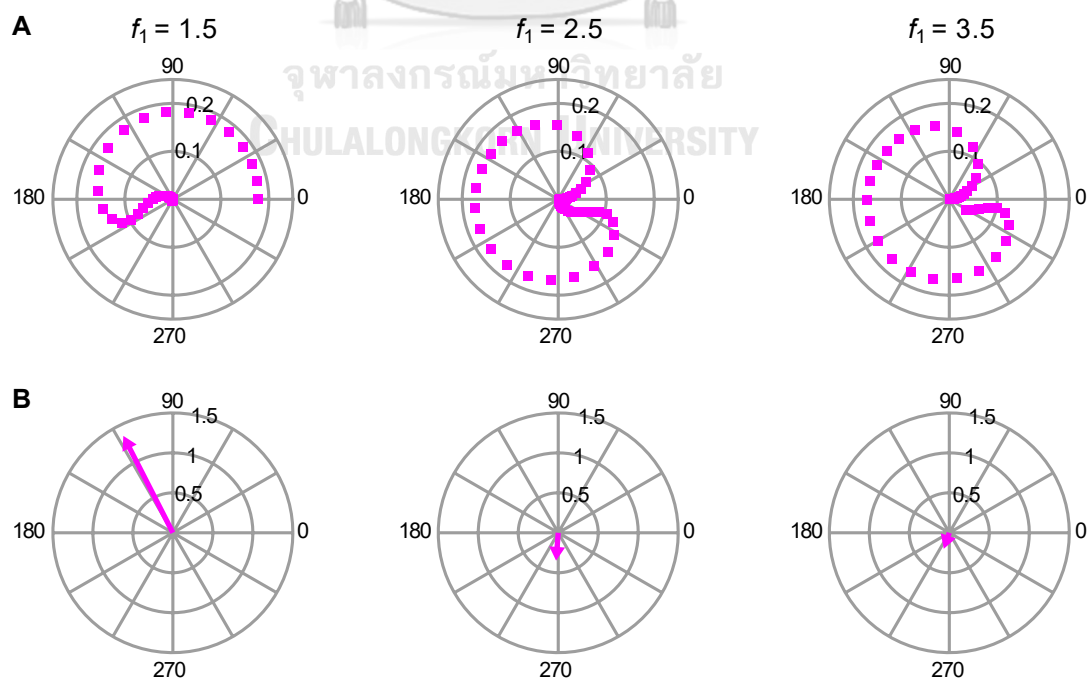


Figure 4.7 Polar plots of oscillator's response.

(A) the individual distortions and (B) the total IMD at $2f_1 - f_2$ from a system of uncoupled oscillators at $F = 6$. From left to right, $f_1 = 1.5, 2.5,$ and 3.5 .

4.4 The total IMDs from a chain of coupled Hopf oscillators

4.4.1 Quasi-periodic amplitude variation pattern

In this section, we modeled the inner ear's sensory organs of bullfrog as a chain of 60 active, nonlinear oscillators, each coupled to its nearest neighbors via elastic elements. For the amphibian papilla, the oscillators were arranged in order of their characteristic frequencies, f_0 , which were uniformly distributed between 1 to 4 to represent the linear tonotopic organization (Fig. 4.5). For the basilar papilla, we represented the non-tonotopic organization by arranging the oscillators in a random order of characteristic frequencies, obtained from a random permutation of the values used in the amphibian papilla case.

With an increase in the driving force amplitude, three distinct features were observed in the total IMDs amplitude at frequency $2f_1 - f_2$. At a weak driving force amplitude, $F = 2$, the level of total IMDs showed multiple local minima and maxima across driving frequencies. At a higher amplitude, $F = 6$, the overall level of total IMDs was enhanced, and a quasi-periodic variation pattern was observed. At $F = 11$, the quasi-periodic pattern persisted, with a broad single peak emerging around stimulus frequency, f_1 , equaled to 1.5. Upon an increase in the amplitude F to 15, the total IMD amplitude at f_1 around 1.5 and 4.4 were enhanced and varied more smoothly with f_1 . At a strong driving force level, $F = 25$, the total IMD showed peaks near f_1 around 1.5 and 4.3 with a small difference between the IMD levels at the peak and notch (Fig. 4.8 A).

For the total IMDs signal at frequency $2f_2 - f_1$, an irregular variation pattern was displayed under weak driving force level, $F = 2$. With an increasing of driving force level, $F = 6$, the variation pattern became more smooth, with a broad peak observed at f_1 around 3.1. Then, after increasing F to 11 and higher, the total IMD profile showed a single peak at f_1 around 3 with an enhancing of an amplitude and slightly shifted from f_1 around 3 to f_1 around 2.5 at $F = 25$ (Fig. 4.8 B).

At very high driving force amplitude, both IMD amplitudes at $2f_1 - f_2$ and $2f_2 - f_1$ (Fig. 4.8 A and B) became nearly identical to the response from uncoupled oscillators (Fig. 4.5 A and B). Our analysis suggested that the distortions produced by each oscillator were dominated by the response at the driving frequencies (Appendix B).

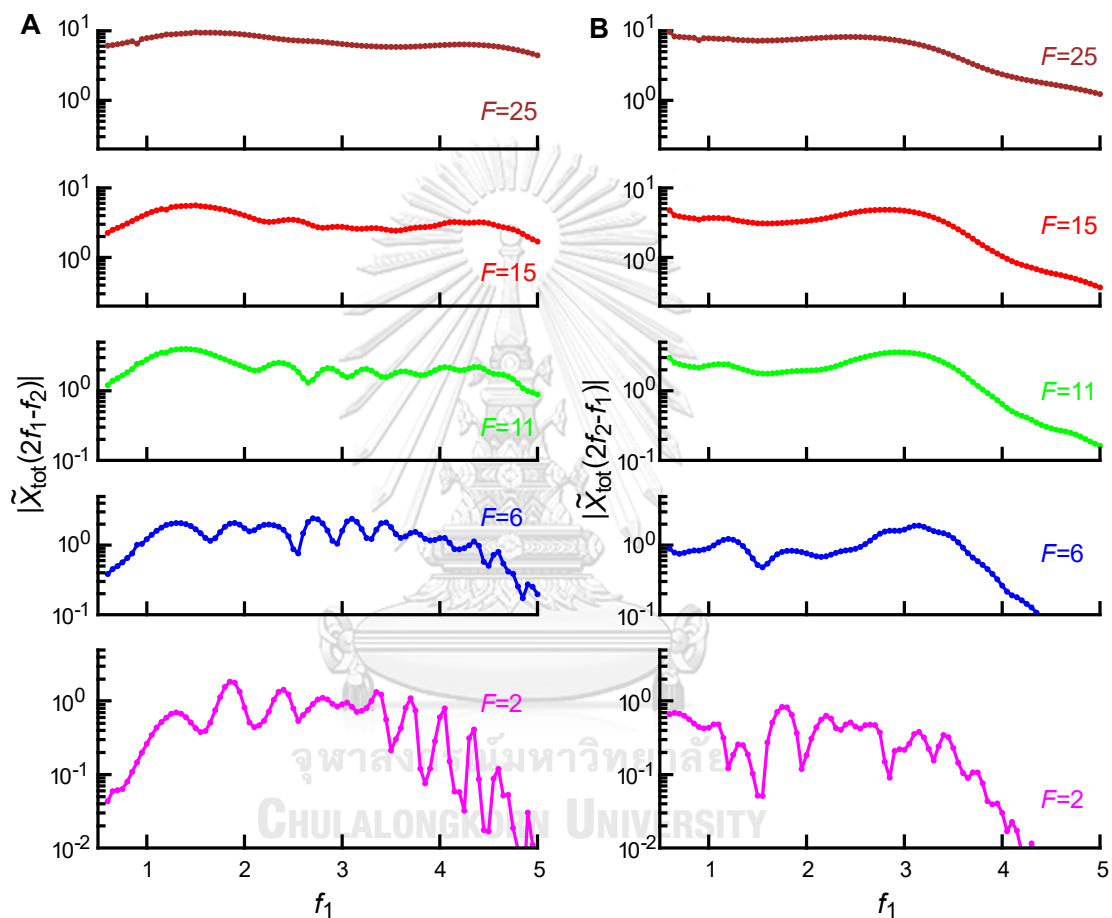


Figure 4.8 Amplitude of total IMDs from a system of coupled oscillators driven by the driving frequency, f_0 , from 0.6 to 5 at (A) $2f_1 - f_2$ and (B) $2f_2 - f_1$ with $d_1 = -60$. From bottom to top, $F = 2$ (magenta), 6 (blue), 11 (green), 15 (red), and 25 (brown).

To investigate how the ripple pattern occurred, the IMD amplitude and phase at frequencies $2f_1 - f_2$ and $2f_2 - f_1$ from each oscillator were plotted against its characteristic frequency (Fig. 4.9 A and B). To illustrate an example of the responses,

we chose the result from driving frequency, f_1 , equal to 3.5. From Fig. 4.9 A, three classes of response were observed depending on the oscillator's characteristic frequency. First, the phase of the IMDs displayed by the oscillators with $f_0 \leq 2f_1 - f_2 - df$ corresponded to a standing wave where the intervals of constant phase were shifted by π rads. The amplitude of the IMDs in this class reached its local maximum when f_0 was at the center of phase plateau and then reached its local minimum at the shifts, comparable with antinodes and nodes of the standing wave.

Second, the phase of the IMDs displayed by the oscillators with $f_0 > 2f_1 - f_2$ varied smoothly with f_0 . The IMDs amplitude in this class showed a similar behavior to the travelling wave found in the response from a system of uncoupled oscillators. Third, the IMDs amplitude and phase displayed by the oscillator within the range $2f_1 - f_2 - df < f_0 < 2f_1 - f_2$ cannot be classified to neither the first nor the second type of vibrational mode.

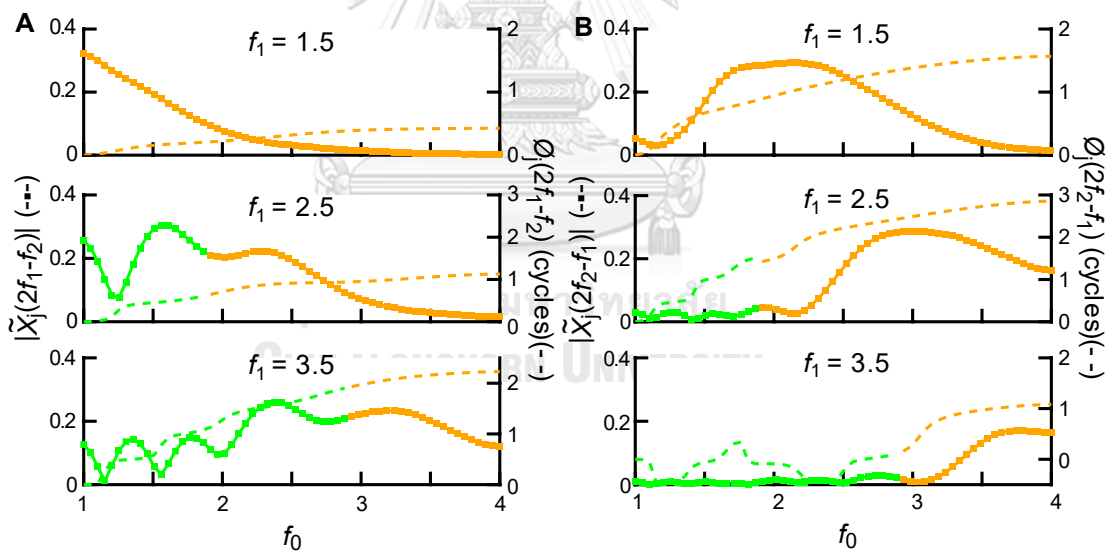


Figure 4.9 Oscillator's response from a system of coupled oscillators.

The individual distortion amplitude (squares) and relative phase (dash lines) at (A) $2f_1 - f_2$ and (B) $2f_2 - f_1$ with $d_1 = -60$ and $F = 11$. Green and orange colors indicate the response from oscillators within the standing wave regime and travelling wave regime, respectively. From top to bottom, $f_1 = 1.5, 2.5,$ and 3.5 .

To simplify the analysis, we categorized the responses into two classes, namely: the coupling regime and the nonlinear regime. Oscillators with characteristic frequencies, f_0 , lower than $2f_1 - f_2$ were classified into a coupling regime, and the others ($f_0 \geq 2f_1 - f_2$) were in a nonlinear regime. The further details for the criterion will be explained in the next section. When the driving frequencies were close to $f_{0,1}$, the response showed only the nonlinear regime. As the driving frequencies were increased, the response that corresponded to the standing wave emerged (Fig. 4.10 B).

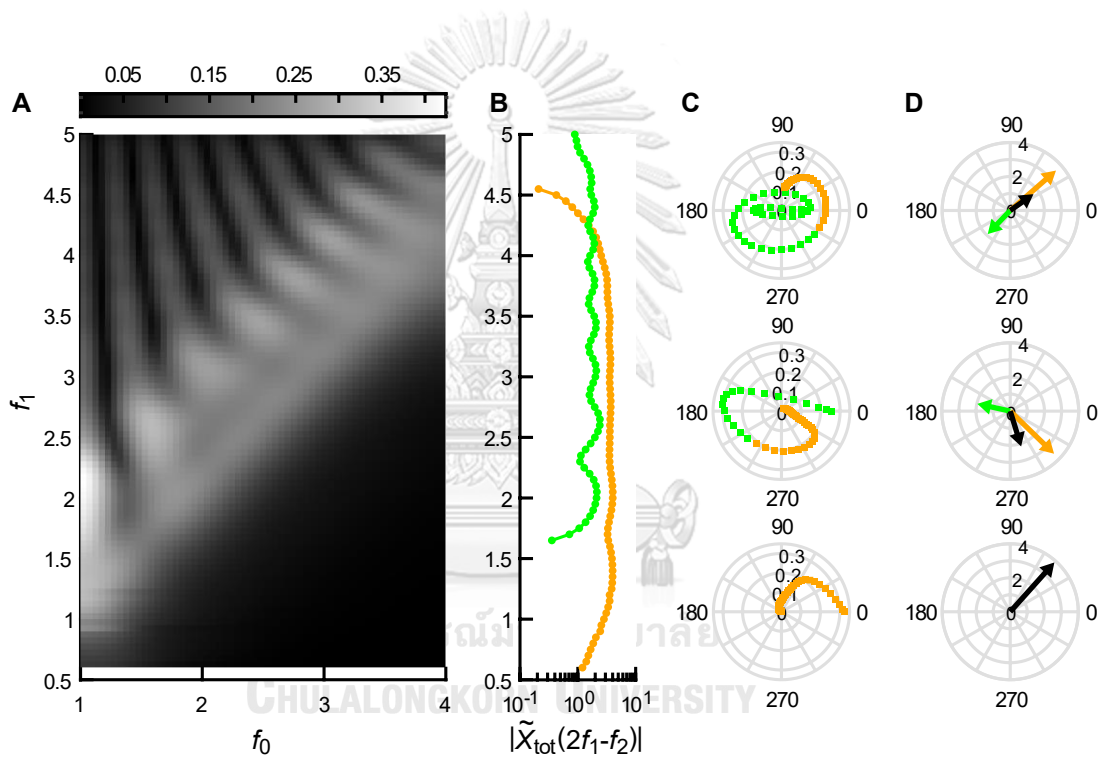


Figure 4.10 The quasiperiodic variation in the IMD amplitude.

At $d_1 = -60$ and $F = 11$. (A) A map of individual distortion amplitude at $2f_1 - f_2$ with a variation of f_1 from 0.6 to 5. Color code indicates an amplitude from low (black) to high (white). (B) The total IMD amplitude at $2f_1 - f_2$ from coupling regime (green) and nonlinear regime (orange). (C) Polar plot of the individual distortion of the oscillators within the coupling regime (green squares) and the nonlinear regime (orange squares). (D) Polar plot of the sum of IMDs from the coupling regime (green arrow), the nonlinear regime (orange arrow) and the total IMD of the system (black arrow) at $2f_1 - f_2$. From bottom to top, $f_1 = 1.5, 2.5, \text{ and } 3.5$.

We investigated the effects of coupling and nonlinear regime on the variation of the total IMD amplitude by representing the IMDs from the oscillators in polar coordinates. The sum of the individual IMDs in each of the two regimes was shown as a vector (Fig. 4.10 C and D).

As the driving frequencies were varied, the number of nodes and antinodes in the standing wave section varied (Fig. 4.10 A). This resulted in a quasiperiodic variation in the magnitude of the total vector sum of the response in the coupling regime (Fig. 4.10 B). In contrast, as the amplitude profile of the response in the nonlinear regime was nearly invariant upon varying the driving frequency, its magnitude of the total vector sum was constant over a broad range of driving frequency. This resulted in the distinct profiles of IMDs amplitude where the coupling regime showed the ripple, but the nonlinear regime remained nearly constant. Note that the total responses from the two regimes were typically nearly out-of-phase. We then concluded that the contribution from the coupling regime gave rise to the quasiperiodic pattern in the total IMD amplitude.

The motion of the chain at the distortion frequency can be explained in the context of the wave that travelling through a free ended string. The distortion signal is primarily generated near the high-frequency end. The wave then traveled toward the low-frequency end where it reflected from the free end, causing the string to have two waves that interference with each other. This resulted in the generation of the standing wave near the low-frequency end of the string. If the oscillators in the system were not coupled, the standing wave could not be generated.

In contrast to the distortion at $2f_1 - f_2$ (Fig. 4.11 A), the coupling regime from the response frequency $2f_2 - f_1$ (Fig. 4.11 B) was considerably weaker. We speculated that this was because the distortion signal had to traverse the part of the chain whose characteristic frequencies were near the stimulus frequencies to reach the low-frequency end. The strong response at the stimulus frequencies displayed by this part of the chain might suppress the distortion signal, rendering the weak standing wave near the low-frequency end. This weak standing wave at $2f_2 - f_1$ corresponded to a smooth variation in its total IMD $2f_2 - f_1$ amplitude.

Moreover, the coupling regime at high driving force magnitudes was attenuated. The nonlinear regime behavior, on the other hand, was enhanced and extended to cover a greater number of oscillators in the system due to an enhancing of amplitude from the response at frequencies f_1 and f_2 (Fig. 4.11 A and B). This was associated with the total IMD amplitude that resembled to a system of uncoupled oscillators.

The response at high driving force magnitudes could be described from the perspective of the response from single oscillators. As a function of driving frequency, the response from each individual oscillator became more broadly tuned. Thus, its IMD would change only minimally upon a slight change in the oscillator's characteristic frequency or the driving frequency. In the chain, this implied that neighboring oscillators, whose characteristic frequencies were only slightly different, should display nearly identical motion at the distortion frequency under strong driving forces. This caused a small difference between their displacements, as well as a minimal force due to the coupling elastic element. This resulted in the response that corresponded to a system of uncoupled oscillators.

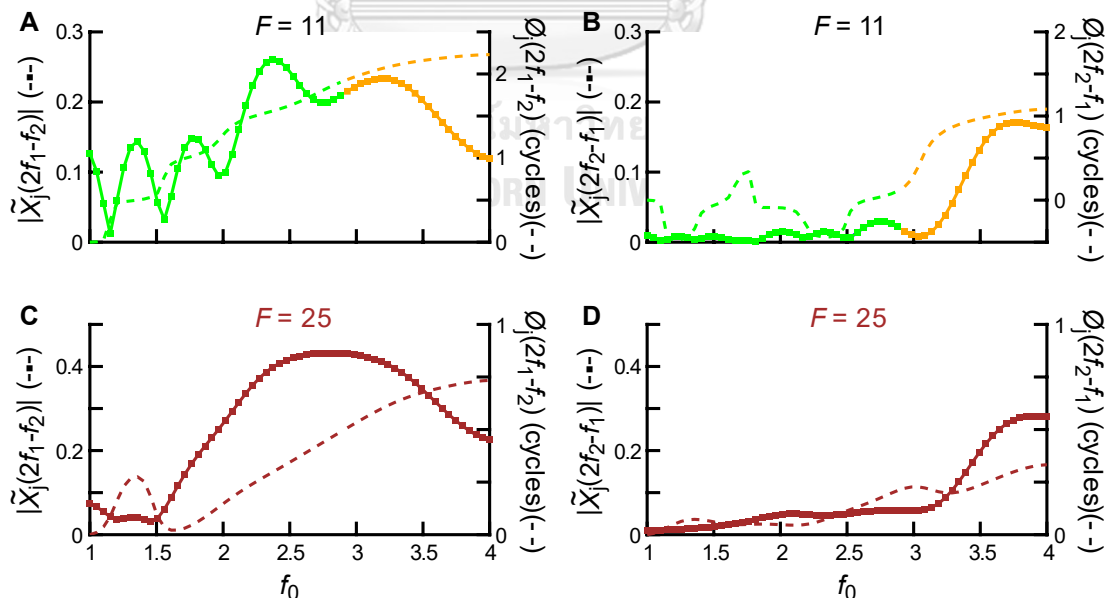


Figure 4.11 Oscillator's response from a different driving forces level.

Comparison between the individual distortion amplitude (squares) and relative phase (dash lines) at (A,C) $2f_1 - f_2$ and (B,D) $2f_2 - f_1$ from a system of coupled

oscillators with $f_1 = 3.5$, $d_I = -60$ and $F = 11$ (A,B) and 25 (C,D). Green and orange color indicates the response from oscillators within the standing wave regime and travelling wave regime, respectively.

4.4.2 Effects of the internal structure of the chain

As demonstrated in the previous section, coupling between oscillators strongly affected the level of total IMDs, as well as those from individual oscillators. The magnitude of coupling force was determined by both stiffness of the elastic elements and the difference in the displacement of neighboring oscillators. To provide more insights into how coupling controlled the individual distortions, an investigation of the effects of the parameters that controlled the coupling force magnitude will be performed in this section. From Equation 3.4, the terms which had strong contributions to the oscillator's velocity at the distortion frequency were the nonlinear term and the coupling term. The magnitude of the coupling term and the nonlinear term were determined from the Fourier component after putting $z_j(t)$ which obtained from numerical simulations into $(d_R + id_I)(z_{j+1}(t) + z_{j-1}(t) - 2z_j(t))$ and $|z_j(t)|^2 z_j(t)$, respectively. The simulations in this section were performed at a fixed driving forces level at 11.

We found that when the standing wave response and the quasiperiodic pattern were observed, the magnitudes of the nonlinear term and the coupling term typically crossed at the oscillator which had its f_0 near $2f_1 - f_2$. (Fig. 4.12 A and 4.13 B) We thus defined the part of the chain containing the oscillators whose f_0 were lower than $2f_1 - f_2$ as the 'coupling regime', and the oscillators with f_0 higher than $2f_1 - f_2$ belonged to the 'nonlinear regime'.

4.4.2.1 Effect of coupling magnitude

At a low d_I , the magnitude of the coupling term for the oscillator which had its f_0 lower than $2f_1 - f_2$ remained at the same level as the nonlinear term. In contrast, a higher d_I enhanced the coupling term, with respect to the nonlinear term (Fig. 4.12 A and B (top)). This behavior was associated with an increase in the magnitude of the response from an oscillator within the coupling regime (Fig. 4.12 A

and B (middle)). The chain displayed a distinct standing-wave pattern with an extended separation between the adjacent node and antinode. This also corresponded to the more pronounced ripples in the total IMD amplitude (Fig. 4.12 A (bottom)). In contrast, the weak coupling magnitude at low d_I could result in the disappearance of the ripple in the total IMD amplitude (Fig. 4.12 B (bottom)).

On the contrary, the magnitude of the nonlinear term from the oscillators in the nonlinear regime, with their f_0 higher than $2f_1 - f_2$, always surpassed the coupling term (Fig. 4.12 A and B (top)). We noticed that the overall magnitude of the response in the nonlinear regime was roughly unaltered upon varying d_I (Fig. 4.12 A and B (middle)).

Our results suggested that an increasing in d_I enhance the magnitude of coupling force between the oscillators. Strong coupling force thus caused the oscillators to synchronize over a broader range, corresponding to the increased wavelength of the standing wave response.

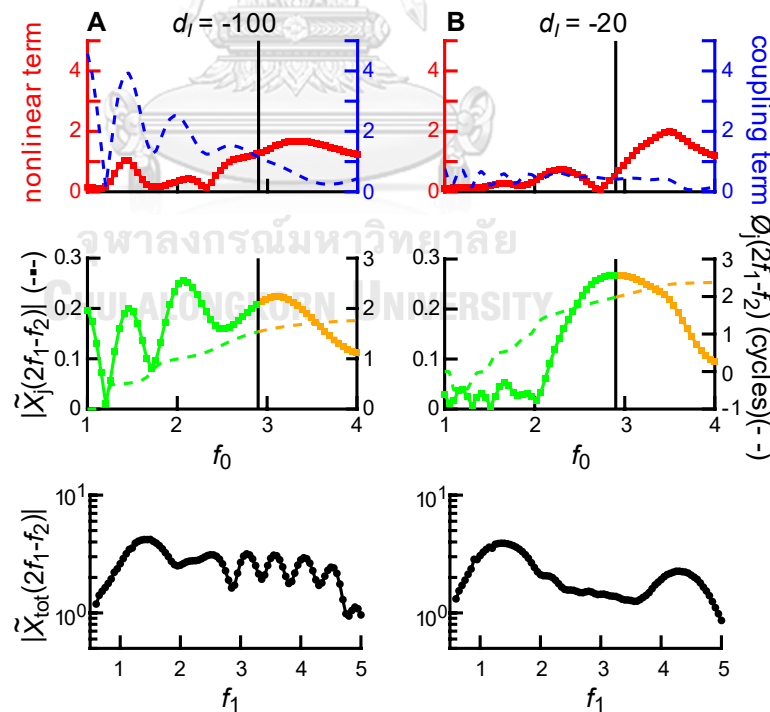


Figure 4.12 Effect of coupling magnitude to a system of coupled oscillators.

In each panel, (top) the magnitude of nonlinear term (squares) and coupling term (blue dash lines) at the distortion frequency $2f_1 - f_2$ from each individual oscillator.

(middle) The individual distortion amplitude (squares) and relative phase (dash lines) at $2f_1 - f_2$ from each individual oscillator. Green and orange squares indicate the response from oscillators within the standing wave regime and travelling wave regime, respectively. Vertical solid line indicates $f_0 = 2f_1 - f_2$. (bottom) The total IMD amplitude at $2f_1 - f_2$ with f_1 from 0.6 to 5. The parameter d_I used in the simulation are (A) -100 and (B) -20.

4.4.4.2 Effect of oscillators number

Next, varying the number of oscillators over a fixed range of characteristic frequencies resulted in the difference of the characteristic frequency between two neighboring oscillators. The simulation results at fixed coupling parameter, $d_I = -60$ and driving frequencies $f_1 = 3.5$ and $f_2 = 4.1$ showed that a smaller number of oscillators increased the magnitude of coupling term from the oscillator which had its f_0 lower than $2f_1 - f_2$, exceeding the nonlinear term. In contrast, a longer chain reduced the magnitude of the coupling term to a level comparable to the nonlinear term (Fig. 4.13 A and B (top)). This decreased the amplitude of the coupling regime (Fig. 4.13 A and B (middle)).

On the contrary, the magnitude of the nonlinear term from the oscillator which had its f_0 higher than $2f_1 - f_2$ showed a similar behavior as the previous section (Fig. 4.13 A and B (top)). This behavior was associated with the response amplitude within the nonlinear regime that remained almost unchanged with the number of oscillators (Fig. 4.13 A and B (middle)).

In association with the weak coupling term observed at a large number of oscillators, the coupling regime amplitude reduced, resulting in the total IMD amplitude that resembled the total IMD from the system of a chain of uncoupled oscillators (Fig. 4.13 A (bottom)). In contrast, a smaller number of oscillators enhanced the response from an oscillator within the coupling regime, corresponding to the distinct rippling pattern in the total IMD amplitude (Fig. 4.13 B (bottom)).

Our results suggested that adding the number of oscillators into the system that had a fixed range of oscillator's characteristic frequencies caused the oscillator to have its characteristic frequency closer to its neighbor, which led to the smaller

relative displacement. This decreased the magnitude of the term $(z_{j+1}(t) + z_{j-1}(t) - 2z_j(t))$, resulting in the reduction in the magnitude of coupling term.

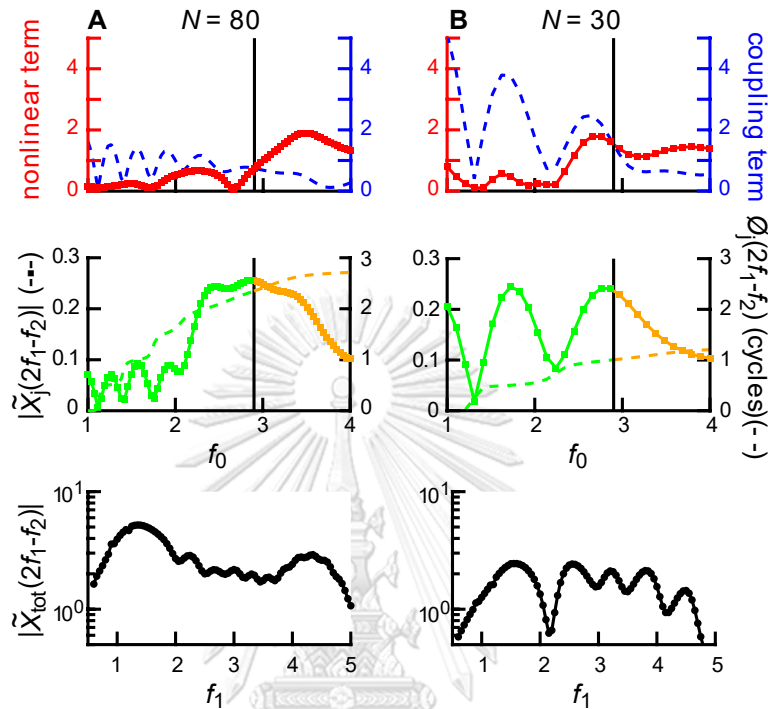


Figure 4.13 Effect of oscillator number to a system of coupled oscillators. In each panel, (top) the magnitude of nonlinear term (red squares) and coupling term (blue dash lines) at the distortion frequency $2f_1 - f_2$ from each individual oscillator. (middle) The individual distortion amplitude (squares) and relative phase (dash lines) at $2f_1 - f_2$ from each individual oscillator. Green and orange squares indicate the response from oscillators within the standing wave regime and travelling wave regime, respectively. Vertical solid line indicates $f_0 = 2f_1 - f_2$. (bottom) The total IMD amplitude at $2f_1 - f_2$ with f_1 from 0.6 to 5. The parameter N used in the simulation are (A) 80 and (B) 30 with $d_1 = -60$.

4.4.2.3 Effect of oscillator's characteristic frequencies organization

Lastly, an investigation of a chain of oscillators with randomly assigned characteristic frequencies. The order of f_0 was obtained from a random permutation of a set of characteristic frequencies used in the previous case. The simulation results showed a broadly tuned peak in the total IMD level at frequency $2f_1 - f_2$ where the

peak centered at the driving frequencies coinciding with the average characteristic frequency of the system (Fig. 4.14 A), similar to the profile of total IMD from single oscillator. With the lack of a tonotopic arrangement, the results showed that the distortion amplitude and relative phase varied independently across the driving frequencies. The phase behavior implied travelling waves with no preferred direction of propagation but appeared localized within the chain. When the driving frequencies were sufficiently higher than the characteristic frequencies of most oscillators, the standing-wave response was found in some parts of the chain (Fig. 4.14 B). This could underlie the ripples observed in the total IMD amplitude observed at high driving frequencies and low driving amplitudes.

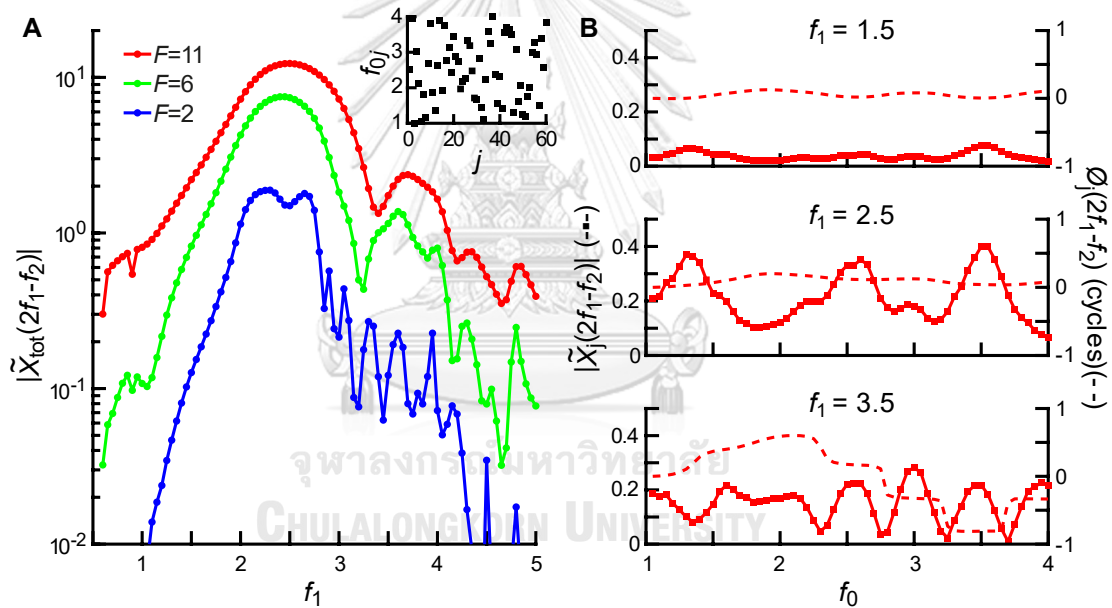


Figure 4.14 Effect of oscillator's characteristic frequencies organization.

(A) Total IMD amplitude at $2f_1 - f_2$ from a system of coupled oscillators with a random arrangement of f_0 and driven by the driving frequency, f_1 , from 0.6 to 5.

From top to bottom, $F = 2$ (blue), 6 (green), and 11 (red). (inset) The profile of oscillator's characteristic frequency used to obtain the data in (A) and (B). (B) The individual distortion amplitude (red squares) and relative phase (red dash lines) at $2f_1 - f_2$. From top to bottom, $f_1 = 1.5, 2.5,$ and 3.5 .

4.5 Comparison with experimental measurements

Simulation results from our investigations are compared with previous experimental measurements of acoustic IMDs emitted from the ears of Chinese edible frogs [7, 25].

Predictions from the model of a chain of coupled oscillators arranged in order of their characteristic frequencies can qualitatively capture the quasi-periodic intensity variation of DPOAEs (Fig. 4.15 A). In the experimental data, this feature is observed between 200 and 1,000 Hz, corresponding to the sensitive frequency range of the amphibian papilla, an organ whose hair cells are arranged tonotopically (Fig. 4.15 B). More specifically, at an appropriate stimulus intensity level, the total IMD profile obtained from the simulations can display multiple notches and peaks across stimulus frequencies. At high stimulus levels, the quasiperiodic pattern disappears, and the total IMD amplitude displays a single maximum.

Results from a chain of coupled oscillators with a random arrangement of their characteristic frequencies show a single broad peak as a function of stimulus frequency (Fig. 4.15 C). The tuning profile remains minimally altered upon changing the driving amplitude. This feature is consistent with the DPOAE intensity levels measured within a frequency range corresponding to the sensitive range of the frog's basilar papilla, between 1,000 and 1,800 Hz (Fig. 4.15 B). Hair cells in the basilar papilla are arranged with no tonotopic organization.

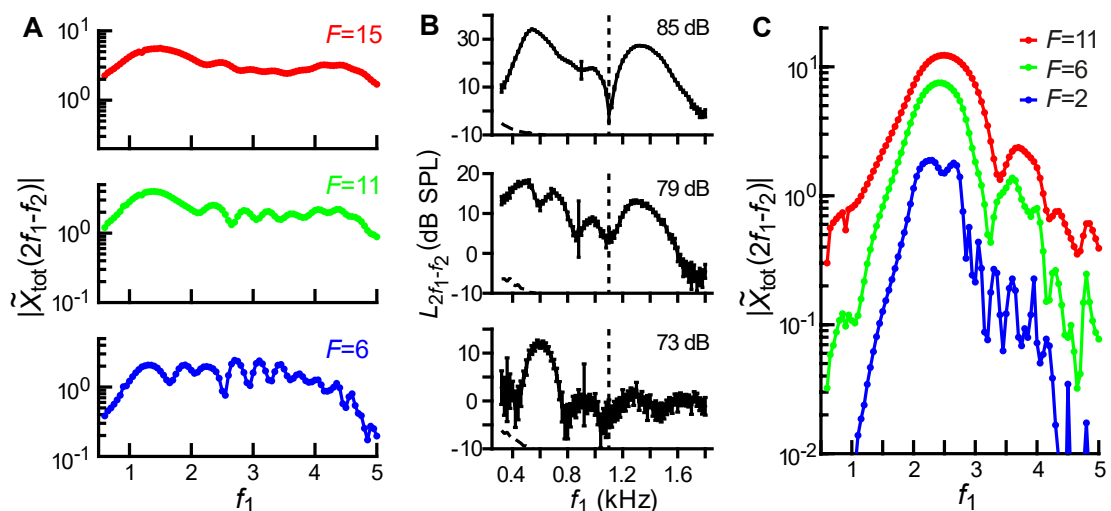


Figure 4.15 Comparison between simulation and experimental results.

(A) Total IMD at $2f_1 - f_2$ from simulation results using a configuration that represent the Chinese edible frog's AP show a quasiperiodic behavior that corresponding to (B) the DPOAE measured from a Chinese edible frog with $f_1 = 0.2$ to 1 kHz. (C) Total IMD at $2f_1 - f_2$ from simulation results using a configuration that represent the Chinese edible frog's BP show a single board peak that corresponding to (B) the DPOAE measured from a Chinese edible frog with $f_1 = 1$ to 1.8 kHz. Vertical dashed lines in (B) indicate the separation of sensitive frequency of Chinese edible frog's AP and BP.

(B) adapted from [25].

4.6 Limitations of the model

Our model assumes that the total IMD response is a linear sum of the contributions from all oscillators. This may not fully represent the DPOAEs measured from the ear canal due to three main reasons.

1. Our model assumes that all oscillators, each representing a hair bundle, are driven by identical driving forces. However, *in vivo* hair bundles are anchored to the overlying structure via elastic elements with different spring constants. Therefore, depending on the stimulus frequencies, some hair bundles may experience weaker driving forces. This distribution in the spring constant also renders unequal contributions of individual oscillators to the total IMD response.

2. The motion of the tectorial structure subsequently elicits the motion of various constituents of the inner ear, including the ossicles and the eardrum within the middle ear, each can impose a bandpass filtering effect. Therefore, the physical properties of these constituents of the ear may alter the magnitudes to the level of IMDs depending on their frequencies. However, our simulation results can qualitatively reproduce the general characteristics of DPOAEs. This suggests that the complex structures of the inner and the middle ear are not mainly responsible for the shape of the intensity profile of the acoustic IMDs emitted from the ear.

However, an addition of physical properties from other components in the internal pathways of the ear may can improve an accuracy of the model.

3. Our model assumes a simple driving force which is independent of the oscillator's displacement. This could be unphysical as in vivo hair bundles are attached to the overlying membrane via an elastic element, and the driving force magnitude is thus presumably governed by the relative displacement of the bundle and the tectorial structure. While adjusting the force terms might have improved our numerical results, a simple force term employed in this model is sufficient to capture the qualitative characteristics of acoustic IMDs from the inner ear.



CHAPTER 5

CONCLUSION

In this study, we performed numerical simulations of IMDs from a chain of active nonlinear oscillators, all driven by identical driving forces of two frequencies. Parameters values used in the model were related to the physiology of the Chinese edible frog inner ear. The results from the model were consistent with previous experimental measurements of DPOAEs from Chinese edible frogs, whose intensity level displayed quasi-periodic variation with stimulus frequency.

To reveal the effects of coupling between oscillators, we first discussed the response from a single nonlinear oscillator which can display a supercritical Hopf bifurcation. The simulation results corresponded to the previous study which indicated that IMDs from single oscillator show a single maximum, with no quasi-periodic behavior observed [4].

Next, the simulations of IMDs at frequency $2f_1 - f_2$ from a system of uncoupled nonlinear oscillators showed that, when arranged oscillators in order of their characteristic frequencies, the displacements of individual oscillators at the distortion frequency corresponded to a travelling wave progressing towards the low-frequency end of the chain. The wave amplitude was broadly tuned with its peak observed at the oscillators whose characteristic frequencies were near the driving frequencies. The wave profile remained unchanged while changing the driving frequencies, resulting in the minimal variation of total IMD amplitude.

Coupling between neighboring oscillators was then introduced. At proper driving force levels and coupling magnitudes, the results was able to qualitatively capture the quasi-periodic behavior in the total IMD amplitude that found from the measurements of DPOAEs from Chinese edible frogs within the frequency range corresponding to the sensitive range of the amphibian papilla. The simulation results of the total IMD amplitude showed multiple local maxima across the driving frequencies, with the frequency separations between each point slightly varying,

resulting in a quasiperiodic pattern. This behavior vanished when the level of the driving forces was sufficiently high. Under weak driving forces, the amplitude variation profile resembled a fluctuation pattern across the driving frequency.

Analyses of the displacements of individual oscillators revealed two types of response which corresponded to a travelling wave and a standing wave. The latter was qualitatively different from the response from an uncoupled chain. The standing wave regime corresponded to the synchronization of oscillators with their neighbors, forming clusters of oscillators that displaced at the same phase. This regime was responsible for the quasiperiodic pattern observed in the amplitude of the total IMD.

The standing- and traveling- wave responses, as well as the quasiperiodic pattern, depended crucially on the arrangement of the oscillators' characteristic frequencies. In the chain that has a random organization of characteristic frequencies, the standing wave was observed when the driving frequencies were suitably higher than the characteristic frequencies of most oscillators in the chain. The traveling wave's amplitude varied nearly randomly along the chain, with no uniform directions of propagation. The results from the random chain were more consistent with the experimental measurements over the range of frequencies corresponding to the frog's basilar papilla, which showed a broadly tuned response.

The effects of the magnitude of driving forces were investigated. The amplitude of the total IMD from both uncoupled and coupled nonlinear oscillators converged at high driving forces levels, and varied smoothly across driving frequencies with no quasiperiodic pattern observed. The response of individual oscillators revealed that this was associated with the attenuated standing-wave response and the enhanced travelling wave. In accordance with the analytical calculation, each oscillator's displacement at the distortion frequency was dominated by its response at the driving frequencies f_1 and f_2 under strong driving forces condition.

In contrast, the contribution of coupling to the oscillator's response at the distortion frequency became significant at lower driving amplitudes. This resulted in an increase in the response amplitude of the oscillators within the standing-wave regime. Our results supported that the quasiperiodic variation in the total-IMD amplitude was originated from the standing-wave response.

The quasiperiodic pattern in the DPOAE intensity variation has been prevalently observed in human subjects. The theory of DPOAE generation from the mammalian cochlea proposed that the fine structure occurred from the interference of the two DPOAE signals produced by two groups of hair cells whose characteristic frequencies coincided with the driving frequencies, and the distortion frequency. However, based on the structure of the inner ear of most lower vertebrate species including frogs, this process was not plausible as the hair cells presumably move in unison as they are anchored tightly to the tectorial membrane which provided a very strong intercellular mechanical coupling. Our theoretical results thus suggested an underlying mechanism for the generation of the quasiperiodic feature in the DPOAE intensity measured from simple inner ears, such as those of frogs. First, most hair cells in the papilla contributed significantly to the distortion response. Second, for an organ in which hair cells were organized in order of their detection frequencies, the motion of low-frequency hair cells could comprise a standing wave that was responsible for the quasiperiodic variation in the DPOAE level.

REFERENCES

1. Rumsey, F. and T. McCormick, *Chapter 18 - Sound Quality*, in *Sound and Recording (Sixth Edition)*, F. Rumsey and T. McCormick, Editors. 2010, Focal Press: Boston. p. 563-590.
2. He, N.J. and R.A. Schmiedt, *Fine structure of the 2f1-f2 acoustic distortion product: changes with primary level*. J Acoust Soc Am, 1993. **94**(5): p. 2659-69.
3. Avan, P., B. Büki, and C. Petit, *Auditory Distortions: Origins and Functions*. Physiological Reviews, 2013. **93**(4): p. 1563-1619.
4. Jülicher, F., D. Andor, and T. Duke, *Physical basis of two-tone interference in hearing*. Proceedings of the National Academy of Sciences, 2001. **98**(16): p. 9080-9085.
5. Barral, J. and P. Martin, *Phantom tones and suppressive masking by active nonlinear oscillation of the hair-cell bundle*. Proceedings of the National Academy of Sciences, 2012. **109**: p. E1344-E1351.
6. Talmadge, C.L., et al., *Experimental confirmation of the two-source interference model for the fine structure of distortion product otoacoustic emissions*. The Journal of the Acoustical Society of America, 1999. **105**(1): p. 275-292.
7. Prawanta, E., et al., *An array of coupled nonlinear oscillators as a model for amplitude variations in intermodulation distortions from the auditory system*. Journal of Physics: Conference Series, 2019. **1380**: p. 012027.
8. Alberti, P.W., *The anatomy and physiology of the ear and hearing*. Occupational exposure to noise: Evaluation, prevention, and control, 2001: p. 53-62.
9. Hudspeth, A.J., *Integrating the active process of hair cells with cochlear function*. Nature Reviews Neuroscience, 2014. **15**(9): p. 600-614.
10. Martin, P., et al., *Spontaneous oscillation by hair bundles of the bullfrog's sacculus*. J Neurosci, 2003. **23**(11): p. 4533-48.
11. Martin, P. and A.J. Hudspeth, *Compressive nonlinearity in the hair bundle's active response to mechanical stimulation*. Proceedings of the National

- Academy of Sciences, 2001. **98**(25): p. 14386-14391.
12. Patel, S.H., et al., *Frequency-selective exocytosis by ribbon synapses of hair cells in the bullfrog's amphibian papilla*. J Neurosci, 2012. **32**(39): p. 13433-8.
 13. Van Dijk, P., et al., *Mechanics of the frog ear*. Hearing research, 2011. **273**(1-2): p. 46-58.
 14. Kung, B.C. and T.O. Willcox, *CHAPTER 25 - EXAMINATION OF HEARING AND BALANCE*, in *Neurology and Clinical Neuroscience*, A.H.V. Schapira, et al., Editors. 2007, Mosby: Philadelphia. p. 318-327.
 15. Mills, D.M., *Interpretation of distortion product otoacoustic emission measurements. I. Two stimulus tones*. J Acoust Soc Am, 1997. **102**(1): p. 413-29.
 16. Prawanta, E., *A STUDY OF ACOUSTIC STIMULATIONS FOR DETECTION OF FINE STRUCTURE OF DISTORTION-PRODUCT OTOACOUSTIC EMISSIONS FROM CHINESE EDIBLE FROG AND NORTH AMERICAN BULLFROG*, in *Department of Physics*. 2019, Chulalongkorn University: Bangkok. p. 24-36.
 17. Eguíluz, V.M., et al., *Essential nonlinearities in hearing*. Phys Rev Lett, 2000. **84**(22): p. 5232-5.
 18. Pikovsky, A., M. Rosenblum, and J. Kurths, *Synchronization : A Universal Concept in Nonlinear Sciences*. The Cambridge Nonlinear Science Series. 2001, Cambridge: Cambridge University Press.
 19. Strogatz, S.H.a., *Nonlinear dynamics and chaos : with applications to physics, biology, chemistry, and engineering*. 2015: Second edition. Boulder, CO : Westview Press, a member of the Perseus Books Group.
 20. Kuznetsov, Y., *Andronov-Hopf bifurcation*. Scholarpedia, 2006. **1**: p. 1858.
 21. Vilfan, A. and T. Duke, *Frequency clustering in spontaneous otoacoustic emissions from a lizard's ear*. Biophysical journal, 2008. **95**(10): p. 4622-4630.
 22. Wit, H.P. and P. van Dijk, *Are human spontaneous otoacoustic emissions generated by a chain of coupled nonlinear oscillators?* J Acoust Soc Am, 2012. **132**(2): p. 918-26.
 23. Wit, H.P., G.A. Manley, and P. van Dijk, *Modeling the characteristics of spontaneous otoacoustic emissions in lizards*. Hearing Research, 2020. **385**: p. 107840.

24. Fruth, F., F. Jülicher, and B. Lindner, *An active oscillator model describes the statistics of spontaneous otoacoustic emissions*. *Biophysical journal*, 2014. **107**(4): p. 815-824.
25. Thipmaungprom, Y., et al., *Auditory intermodulation distortions from an array of active nonlinear oscillators*. 2021. Manuscript submitted for publication.





APPENDIX

จุฬาลงกรณ์มหาวิทยาลัย
CHULALONGKORN UNIVERSITY

APPENDIX A

Calculation of IMDs from a single Hopf oscillator

We perform an analytical approximation of the intermodulation distortions displayed by a single Hopf oscillator.

$$\dot{Z} = (\mu + i\omega_0)Z - |Z|^2Z + F(t) \quad (\text{AA.1})$$

with the force term

$$F(t) = F_{f_1} e^{i2\pi f_1 t} + F_{f_2} e^{i2\pi f_2 t} \quad (\text{AA.2})$$

the response of an oscillator contained all Fourier components at frequencies $f = mf_1 + nf_2$, where m and n are positive or negative integers. Then, the response can be written as

$$X(t) = \sum_k X_{f_k} e^{i2\pi f_k t} \quad (\text{AA.3})$$

where $f_k = f_1 + (k-1)\Delta f$ and $\Delta f = f_2 - f_1$

For small forcing amplitudes, expand the variable $Z(t)$ as

$$Z = R_1 e^{i2\pi f_1 t + i\phi_1} + R_2 e^{i2\pi f_2 t + i\phi_2} + R_{12} e^{i2\pi f_{12} t + i\phi_{12}} + R_{21} e^{i2\pi f_{21} t + i\phi_{21}} \quad (\text{AA.4})$$

where $f_{12} = (2f_2 - f_1)$, $f_{21} = (2f_1 - f_2)$, ϕ_{12} is phase at frequency $2f_2 - f_1$, and ϕ_{21} is phase at frequency $2f_1 - f_2$ with an assumption that the response at other frequencies has very low amplitude compare to those corresponding to frequencies f_1 , f_2 , $2f_1 - f_2$, and $2f_2 - f_1$, based on the results from [4, 5].

Consider the term $|Z|^2Z$, we can write

$$\begin{aligned} |Z|^2Z = & [R_1 e^{i\omega_1 t + i\phi_1} + R_2 e^{i\omega_2 t + i\phi_2} + R_{12} e^{i\omega_{12} t + i\phi_{12}} + \\ & R_{21} e^{i\omega_{21} t + i\phi_{21}}] [R_1^* e^{-i\omega_1 t - i\phi_1} + R_2^* e^{-i\omega_2 t - i\phi_2} + \\ & R_{12}^* e^{-i\omega_{12} t - i\phi_{12}} + R_{21}^* e^{-i\omega_{21} t - i\phi_{21}}] [R_1 e^{i\omega_1 t + i\phi_1} + \\ & R_2 e^{i\omega_2 t + i\phi_2} + R_{12} e^{i\omega_{12} t + i\phi_{12}} + R_{21} e^{i\omega_{21} t + i\phi_{21}}]. \end{aligned} \quad (\text{AA.5})$$

To evaluate the response at frequency $2f_1 - f_2$, we keep the terms with f_{21} .

Then equation AA.5 gives

$$\begin{aligned} |Z|^2Z = & R_1^2 R_2 e^{i2\pi f_{21} t + i(2\phi_1 - \phi_2)} + [R_1^2 R_{21} + R_2^2 R_{21} + R_{12}^2 R_{21} + \\ & R_{21}^2 R_{21}] e^{i2\pi f_{21} t + i\phi_{21}} \end{aligned} \quad (\text{AA.6})$$

Plugging equation AA.4 and AA.6 back to equation AA.1 and keep only the terms with $f = f_{21}$, we obtain

$$i2\pi f_{21} R_{21} e^{i2\pi f_{21} t + i\phi_{21}} = (\mu + i2\pi f_0) R_{21} e^{i2\pi f_{21} t + i\phi_{21}} - R_1^2 R_2 e^{i2\pi f_{21} t + i(2\phi_1 - \phi_2)} - [R_1^2 R_{21} + R_2^2 R_{21} + R_{12}^2 R_{21} + R_{21}^2 R_{21}] e^{i2\pi f_{21} t + i\phi_{21}} \quad (\text{AA.7})$$

which gives

$$i2\pi f_{21} R_{21} = (\mu + i2\pi f_0) R_{21} - R_1^2 R_2 e^{i(2\phi_1 - \phi_2 - \phi_{21})} - [R_1^2 R_{21} + R_2^2 R_{21} + R_{12}^2 R_{21} + R_{21}^2 R_{21}] \quad (\text{AA.8})$$

Separating equation AA.8 into real and imaginary part, we show that

$$R_1^2 R_2 \cos(2\phi_1 - \phi_2 - \phi_{21}) = -[R_1^2 R_{21} + R_2^2 R_{21} + R_{12}^2 R_{21} + R_{21}^2 R_{21}] - \mu R_{21} \quad (\text{AA.9})$$

for the real part and

$$R_1^2 R_2 \sin(2\phi_1 - \phi_2 - \phi_{21}) = -2\pi f_{21} R_{21} + 2\pi f_0 R_{21} \quad (\text{AA.10})$$

for the imaginary part.

After summing the square of equation AA.9 and AA.10, we obtain

$$R_{21} = R_1^2 R_2 [(R_1^2 + R_2^2 + R_{12}^2 + R_{21}^2 - \mu)^2 + (2\pi f_{21} - 2\pi f_0)^2]^{-1/2} \quad (\text{AA.11})$$

Equations AA.11 indicates that the response at $2f_1 - f_2$ arises from the response at the driving frequencies f_1 and f_2 , even when the external force does not contain a component at the distortion frequency.

Next, to obtain a closed form for the phase of the distortion, we divide equation AA.10 by equation AA.9

$$\tan(2\phi_1 - \phi_2 - \phi_{21}) = \frac{2\pi f_{21} - 2\pi f_0}{[R_1^2 + R_2^2 + R_{12}^2 + R_{21}^2] - \mu}$$

which can be rewritten as

$$\phi_{21} = 2\phi_1 - \phi_2 - \arctan \left[\frac{2\pi f_{21} - 2\pi f_0}{[R_1^2 + R_2^2 + R_{12}^2 + R_{21}^2] - \mu} \right] \quad (\text{AA.12})$$

Equations AA.11 and AA.12 show the amplitude and phase of the distortion at $2f_1 - f_2$ as functions of the response at frequencies f_1 , f_2 , and $2f_2 - f_1$. Next, we evaluate the oscillator's displacement at the driving frequencies f_1 and f_2 . From equation AA.5, we consider the terms with f_1 . One can show that

$$i2\pi f_1 R_1 e^{i\omega_1 t + i\phi_1} = (\mu + i2\pi f_0) R_1 e^{i2\pi f_1 t + i\phi_1} - R_1^2 R_1 e^{i2\pi f_1 t + i\phi_1} - 2R_2^2 R_1 e^{i2\pi f_1 t + i\phi_1} - 2R_{mn}^2 R_1 e^{i2\pi f_1 t + i\phi_1} + F_1 e^{i2\pi f_1 t}$$

which becomes

$$i2\pi f_1 R_1 = (\mu + i2\pi f_0)R_1 - R_1^2 R_1 - 2R_2^2 R_1 - 2R_{mn}^2 R_1 + F_1 e^{-i\phi_1}. \quad (\text{AA.13})$$

The real part of equation AA.13 reads

$$F_1 \cos(-\phi_1) = \mu R_1 - R_1^2 R_1 - 2R_2^2 R_1 - 2R_{mn}^2 R_1, \quad (\text{AA.14})$$

whereas the imaginary part satisfies

$$F_1 \sin(-\phi_1) = 2\pi f_0 R_1 - 2\pi f_1 R_1. \quad (\text{AA.15})$$

The sum of the squares of equation AA.13 and AA.14 gives the relation of an amplitude of the response at frequency f_1 to the driving force

$$F_1 = R_1 [(2\pi f_1 - 2\pi f_0)^2 + (R_1^2 + 2R_2^2 + 2R_{mn}^2 - \mu)^2]^{1/2}. \quad (\text{AA.16})$$

Divided equation AA.15 by equation AA.14, we obtain

$$\tan(-\phi_1) = \frac{2\pi f_0 - 2\pi f_1}{R_1^2 + 2R_2^2 + 2R_{mn}^2 - \mu}$$

which gives the relation of phase of the response at frequency f_1 to the driving force

$$\phi_1 = -\arctan \left[\frac{2\pi f_0 - 2\pi f_1}{R_1^2 + 2R_2^2 + 2R_{mn}^2 - \mu} \right] \quad (\text{AA.17})$$

If F_2 becomes 0 with $\mu \sim 0$ and $\omega_1 \sim \omega_0$, equation AA.16 can be written as $F_1 \sim R_1^3$.

Similarly, the response at frequency f_2 can be obtained by keeping the terms with $f = f_2$ in $|Z|^2 Z$. One can show that

$$0 = \mu R_2 - R_2^2 R_2 - 2R_1^2 R_2 - 2R_{mn}^2 R_2 + F_2 \cos(-\phi_2) \quad (\text{AA.18})$$

and

$$2\pi f_2 R_2 = 2\pi f_0 R_2 - F_2 \sin(-\phi_2). \quad (\text{AA.19})$$

After using the same method as we used to obtain the relation of amplitude and phase with the driving force at frequency f_1 , we show that

$$F_2 = R_2 [(\omega_2 - \omega_0)^2 + (R_2^2 + 2R_1^2 + 2R_{mn}^2 - \mu)^2]^{1/2} \quad (\text{AA.20})$$

and

$$\phi_2 = -\arctan \left[\frac{2\pi f_0 - 2\pi f_2}{R_2^2 + 2R_1^2 + 2R_{mn}^2 - \mu} \right] \quad (\text{AA.21})$$

Equations AA.11, AA.12, AA.16, AA.17, AA.20, and AA.21 show that the displacement of the oscillator at a certain frequency is always influenced by the response at other frequencies. If we assume that R_{21} and R_{12} are much smaller than R_1 and R_2 , Equation AA.16, AA.17, AA.20, and AA.21 become

$$F_1 = R_1[(2\pi f_1 - 2\pi f_0)^2 + (R_1^2 + 2R_2^2 - \mu)^2]^{1/2} \quad (\text{AA.22})$$

$$\phi_1 = -\arctan \left[\frac{2\pi f_0 - 2\pi f_1}{R_1^2 + 2R_2^2 - \mu} \right] \quad (\text{AA.23})$$

$$F_2 = R_2[(2\pi f_2 - 2\pi f_0)^2 + (R_2^2 + 2R_1^2 - \mu)^2]^{1/2} \quad (\text{AA.24})$$

$$\phi_2 = -\arctan \left[\frac{2\pi f_0 - 2\pi f_2}{R_2^2 + 2R_1^2 - \mu} \right] \quad (\text{AA.25})$$

respectively.

An IMD amplitude can be obtained by putting equation AA.22, AA.23, AA.24, and AA.25 into AA.11. If we assume that R_{21} and R_{12} are much smaller than R_1 and R_2 , $\mu = 0$, and $2\pi f_1$ and $2\pi f_2 \sim 2\pi f_0$, we can obtain the relation $R_{21} \sim R_1^2 R_2 [R_1^2 + R_2^2]^{-1/2}$ from equation AA.11. Our results thus predict a global maximum in IMD amplitude since equation AA.22 shows that R_1 and R_2 reach their global maximum when $2\pi f_1 \sim 2\pi f_0$.

APPENDIX B

Calculation of intermodulation distortion from a chain of coupled Hopf oscillators

Firstly, to get an equation that can describe intermodulation distortion from a chain of Hopf oscillators, we modify the force term of equation 3.4 to

$$\dot{Z}_j = (\mu_j + i2\pi f_{0j})Z_j - |Z_j|^2 Z_j + (d_R + id_I)(Z_{j+1} + Z_{j-1} - 2Z_j) + F(t). \quad (\text{AB.1})$$

We use the driving force term in the same form as we used in equation AA.2 for convenience. By using the solution

$$Z_j = R_{1j}e^{i2\pi f_{1j}t+i\phi_{1j}} + R_{2j}e^{i2\pi f_{2j}t+i\phi_{2j}} + R_{12j}e^{i2\pi f_{12j}t+i\phi_{12j}} + R_{21j}e^{i2\pi f_{21j}t+i\phi_{21j}} \quad (\text{AB.2})$$

with an assumption that the response at other frequencies has very low amplitude compared to f_1 , f_2 , $2f_1 - f_2$, and $2f_2 - f_1$.

Consider the term $|Z_j|^2 Z_j$, we got

$$\begin{aligned} |Z_j|^2 Z_j = & [R_{1j}e^{i2\pi f_{1j}t+i\phi_{1j}} + R_{2j}e^{i2\pi f_{2j}t+i\phi_{2j}} + R_{12j}e^{i2\pi f_{12j}t+i\phi_{12j}} + \\ & R_{21j}e^{i2\pi f_{21j}t+i\phi_{21j}}][R_{1j}^*e^{-i2\pi f_{1j}t-i\phi_{1j}} + \\ & R_{2j}^*e^{-i2\pi f_{2j}t-i\phi_{2j}} + R_{12j}^*e^{-i2\pi f_{12j}t-i\phi_{12j}} + \\ & R_{21j}^*e^{-i2\pi f_{21j}t-i\phi_{21j}}][R_{1j}e^{i2\pi f_{1j}t+i\phi_{1j}} + R_{2j}e^{i2\pi f_{2j}t+i\phi_{2j}} + \\ & R_{12j}e^{i2\pi f_{12j}t+i\phi_{12j}} + R_{21j}e^{i2\pi f_{21j}t+i\phi_{21j}}]. \end{aligned} \quad (\text{AB.3})$$

To see the response at frequency $2f_1 - f_2$, we keep only terms that have f_{21j} .

Then equation AB.3 gives

$$\begin{aligned} |Z_j|^2 Z_j = & R_{1j}^2 R_{2j} e^{i2\pi f_{21j}t+i(2\phi_{1j}-\phi_{2j})} + [R_{1j}^2 R_{21j} + R_{2j}^2 R_{21j} + \\ & R_{12j}^2 R_{21j} + R_{21j}^2 R_{21j}] e^{i\omega_{21j}t+i\phi_{21j}} \end{aligned} \quad (\text{AB.4})$$

Putting equation AB.2 and AB.4 back to equation AB.1 and keeping only terms that have f_{21j} , we get

$$\begin{aligned} i2\pi f_{21j} R_{21j} e^{i2\pi f_{21j}t+i\phi_{21j}} = & (\mu_j + i2\pi f_{0j}) R_{21j} e^{i2\pi f_{21j}t+i\phi_{21j}} - \\ & R_{1j}^2 R_{2j} e^{i2\pi f_{21j}t+i(2\phi_{1j}-\phi_{2j})} - [R_{1j}^2 R_{21j} + R_{2j}^2 R_{21j} + R_{12j}^2 R_{21j} + \\ & R_{21j}^2 R_{21j}] e^{i2\pi f_{21j}t+i\phi_{21j}} + (d_R + id_I)[R_{21j+1} e^{i2\pi f_{21j+1}t+i\phi_{21j+1}} + \\ & R_{21j-1} e^{i2\pi f_{21j-1}t+i\phi_{21j-1}} - 2R_{21j} e^{i2\pi f_{21j}t+i\phi_{21j}}] \end{aligned} \quad (\text{AB.5})$$

which give

$$\begin{aligned}
i2\pi f_{21j}R_{21j} = & (\mu_j + i2\pi f_{0j})R_{21j} - R_{1j}^2R_{2j}e^{i(2\phi_{1j}-\phi_{2j}-\phi_{21j})} - \\
& [R_{1j}^2 + R_{2j}^2 + R_{12j}^2 + R_{21j}^2]R_{21j} + (d_R + \\
& id_I)[R_{21j+1}e^{i(2\pi f_{21j+1}-2\pi f_{21j})t+i(\phi_{21j+1}-\phi_{21j})} + \\
& R_{21j-1}e^{i(2\pi f_{21j-1}-2\pi f_{21j})t+i(\phi_{21j-1}-\phi_{21j})} - 2R_{21j}]
\end{aligned} \tag{AB.6}$$

Separating equation AB.6 into real and imaginary part, we get

$$\begin{aligned}
0 = & \mu_jR_{21j} - R_{1j}^2R_{2j}\cos(2\phi_{1j} - \phi_{2j} - \phi_{21j}) - [R_{1j}^2 + R_{2j}^2 + R_{12j}^2 + \\
& R_{21j}^2]R_{21j} + d_R[R_{21j+1}\cos((2\pi f_{21j+1} - 2\pi f_{21j})t + (\phi_{21j+1} - \\
& \phi_{21j})) + R_{21j-1}\cos((2\pi f_{21j-1} - 2\pi f_{21j})t + (\phi_{21j-1} - \phi_{21j})) - \\
& 2R_{21j}] - d_I[R_{21j+1}\sin((2\pi f_{21j+1} - 2\pi f_{21j})t + (\phi_{21j+1} - \\
& \phi_{21j})) + R_{21j-1}\sin((2\pi f_{21j-1} - 2\pi f_{21j})t + (\phi_{21j-1} - \phi_{21j}))]
\end{aligned} \tag{AB.7}$$

for the real part and

$$\begin{aligned}
2\pi f_{21j}R_{21j} = & 2\pi f_{0j}R_{21j} - R_{1j}^2R_{2j}\sin(2\phi_{1j} - \phi_{2j} - \phi_{21j}) + \\
& d_R[R_{21j+1}\sin((2\pi f_{21j+1} - 2\pi f_{21j})t + (\phi_{21j+1} - \\
& \phi_{21j})) + R_{21j-1}\sin((2\pi f_{21j-1} - 2\pi f_{21j})t + (\phi_{21j-1} - \\
& \phi_{21j}))] + d_I[R_{21j+1}\cos((2\pi f_{21j+1} - 2\pi f_{21j})t + \\
& (\phi_{21j+1} - \phi_{21j})) + R_{21j-1}\cos((2\pi f_{21j-1} - 2\pi f_{21j})t + \\
& (\phi_{21j-1} - \phi_{21j})) - 2R_{21j}]
\end{aligned} \tag{AB.8}$$

for the imaginary part.

Both of equations AB.7 and AB.8 cannot be solved analytically. However, they suggest that in a strong driving force limit, in which the response at frequencies f_1 and f_2 dominate the response at the distortion frequencies, the terms involving coupling become more negligible. This leads to the total response that similar to a chain of non-coupled oscillators.

VITA

NAME Yanathip Thipmaungprom

DATE OF BIRTH 17 December 1995



จุฬาลงกรณ์มหาวิทยาลัย
CHULALONGKORN UNIVERSITY